Measurement of orientation and alignment moment relaxation by polarization spectroscopy: Theory and experiment

Matthew L. Costen, Hilary J. Crichton, and Kenneth G. McKendrick

Citation: The Journal of Chemical Physics **120**, 7910 (2004); doi: 10.1063/1.1691019
View online: http://dx.doi.org/10.1063/1.1691019
View Table of Contents: http://scitation.aip.org/content/aip/journal/jcp/120/17?ver=pdfcov
Published by the AIP Publishing

Measurement of orientation and alignment moment relaxation by polarization spectroscopy: Theory and experiment

Matthew L. Costen,[a] Hilary J. Crichton, and Kenneth G. McKendrick
School of Engineering and Physical Sciences, William H. Perkin Building, Heriot-Watt University, Edinburgh, EH14 4AS, United Kingdom

(Received 23 October 2003; accepted 9 February 2004)

A diagrammatic perturbation theory description of one-color polarization spectroscopy (PS) is developed which emphasizes the significance of orientation and alignment tensor moments of the rotational angular momentum, and their collisional evolution. The influences of Doppler motion, velocity-changing collisions, decay of population, orientation and alignment, and nuclear hyperfine depolarization on the calculated PS signal are discussed. Illustrative simulations are presented of the evolution of the PS signal as a function of pump–probe laser delay. These are generated by a Monte Carlo integration of the derived equations for the signal electric field over typical experimental pump and probe laser temporal profiles and velocity distributions for a commonly studied system, the OH $A\,^2\Sigma^+ - X\,^2\Pi$ (0,0) band. These predictions are compared with a preliminary set of results obtained in an experimental apparatus designed for one-color polarization spectroscopy using independent pump and probe lasers. Measurements are presented using linearly polarized pump light on the $Q_1(2.5)$ transition of the OH $A\,^2\Sigma^+ - X\,^2\Pi$ (0,0) band with He as the collision partner. The decay of the experimental PS pump–probe signal is discussed with reference to inelastic collisional population transfer rates in the literature. It is concluded that the collisional depolarization of rotational alignment is rapid, with a rate approximately twice that of population transfer. This is consistent with previous measurements in atmospheric pressure flames. PS is shown to be a viable novel spectroscopic method for determining rotational angular momentum orientation and alignment relaxation rates, which are valuable quantities because they are sensitive probes of the forces involved in inelastic collisions.
[DOI: 10.1063/1.1691019]

I. INTRODUCTION

Polarization spectroscopy (PS) was first developed by Hänsch and co-workers[1] as a variant of saturation spectroscopy. In its simplest form, a relatively powerful polarized pump laser beam is introduced to the sample, creating an unequal m_J distribution in the ground and excited levels connected by the transition. A weaker linearly polarized probe laser beam, also resonant with the transition, is then co- or counterpropagated with the pump beam. A signal beam is generated which copropagates with the probe beam, but has an orthogonal linear polarization. The signal beam is separated from the probe beam using a linear polarizer. In the last 10 years, PS has seen increasing use in analytical measurements in bright or collisionally perturbed environments where the coherent signal beam properties are useful. These have included a significant number of studies of small radicals in flames, notably OH,[2,3] NH,[4] NO,[5] and C_2.[6] This work has mainly focused on the use of PS for relative and absolute concentration measurements, along with the determination of rotational temperatures.

There have been a number of recent papers describing a numerical approach to the simulation of PS suitable for the strong field regime. Perhaps the most significant of these, by Reichardt, Lucht, and co-workers,[7] used a numerical solution to the time-dependent density matrices. These calculations included collisional effects and Doppler broadening, and the line shapes and saturation effects that result were discussed. Further publications discussed the effects of multiaxial laser modes[8] and short pulse (picosecond) lasers.[9] The results of such calculations have been compared to measurements made in flames using saturated PS on known concentrations of OH, with good agreement being found.[10]

The collisional properties of PS have been the subject of fewer studies. Reichardt *et al.*[11] have presented a diagrammatic perturbative treatment of PS in which they describe the laser pulses as exponentially decaying temporal functions. They present analytical results for PS signal intensity as a function of collision rate for the case where pump and probe pulses are coincident in time. They show a decreased dependence on collision rate for a short pulse ps-laser over the longer pulses from a ns-pulsed laser. The effect of collisions on PS is most clearly seen when the relative timings of the pump and probe laser pulses are varied. The relaxation times of PS signals from OH in atmospheric pressure flames using picosecond laser pulses have been measured.[12–15] The reported relaxation times are rapid, 120–700 ps, and depend on J and pump polarization. The results were interpreted in a perturbative theory approach, assuming that the probe pulse only switched on after the pump pulse finished, and that the

[a]Author to whom correspondence should be addressed. Electronic mail: M.L.Costen@hw.ac.uk

pump and probe pulses were short compared to the relaxation time scale.

We have been developing PS as a tool for studying inelastic energy transfer of small radicals.[16] We are interested in the evolution of the orientation and alignment of rotational angular momentum in the course of inelastic collisions. These have been shown in both reactive and inelastic scattering to be a sensitive probe of the forces involved in the collision.[17] For example, in perhaps the most sophisticated of the recent applications of related methods to nonreactive collisions, measurements of the orientation and alignment of NO ($X\,^2\Pi$) created in collisions with Ar have been obtained using crossed molecular beams with REMPI-TOF imaging detection.[18,19] Deviations from the simple predictions of the kinematic apse model were seen, in particular a preferential handedness of rotation as a function of scattering angle, illustrating the depth of information that can be revealed.

We are particularly interested in electronically inelastic collisions, and have recently been studying transfer between the $A\,^2\Delta$ and $B\,^2\Sigma$ states of CH.[20] Those experiments involved pulsed laser preparation of single rotational levels in either of the electronic states, followed by dispersed fluorescence resolution of the post collision state distribution at the rotational level.[21] We have observed rapid transfer between electronic states with a variety of colliders.[22] Simple models, that may be successful in explaining purely rotationally inelastic collisions, do not correctly predict the observed propensities for transfer or final state distributions in these electronic state-changing collisions. Development of more successful models would seem to require better information on the forces acting in the collisions. Rotational angular momentum alignment provides just such a detailed window on the forces present.

However, measurements of changes in orientation and alignment in collisions of excited state species are very rare. This is largely due to the lack of higher-lying excited states suitable for conventional optical double-resonance experiments in these small free radicals. We have therefore been searching for a technique that will allow polarization-sensitive detection without requiring such higher states. We believe that polarization spectroscopy provides such a method. In an earlier paper,[16] we demonstrated excellent signal to noise in one-color PS of the OH $A\,^2\Sigma^+ - X\,^2\Pi$ transition, under controlled collider conditions in a sealed environment. In those experiments, a single ns-pulsed laser was used to generate both pump and probe pulses, which were essentially coincident in time. The effects of collisions on the PS signal were explored by increasing the partial pressure of collider gas. Very rapid decay rates for the PS signal were found, which it was suggested might be the result of velocity-changing collisions. Here we develop the theoretical framework for the general analysis of one-color PS signals with arbitrary pump–probe delay and demonstrate the application of the method to an illustrative set of new measurements for OH.

II. THEORETICAL DESCRIPTION OF PS

A. Introduction

Polarization spectroscopy is a third order non-linear spectroscopy, a variant of four wave mixing (FWM).[23] FWM in general arises from the interaction of three beams with a polarizable medium, the nonlinear polarization induced in the medium producing a fourth coherent signal beam. This signal beam will propagate in a direction determined by the phase matching conditions operating on the wave vectors of the input beams. In PS there are only two independent input beams (pump and probe) and the signal beam is detected in the same propagation direction as the probe beam. The wave vector for the signal beam is required to be the same as the probe beam, $\mathbf{k}_{\text{signal}}=\mathbf{k}_{\text{probe}}$, and hence two photons from the pump beam must be used such that $\mathbf{k}_{\text{signal}}=\mathbf{k}_{\text{probe}}+\mathbf{k}_{\text{pump}}-\mathbf{k}_{\text{pump}}$. All calculations in this paper are made under an assumption that the pump and probe beams copropagate. A number of other possible third order processes may occur in the sample under the influence of these laser fields, for example, coherent anti-Stokes Raman spectroscopy (CARS) and degenerate four wave mixing (DWFM). These result in various different signal beams, propagating in various possible directions and with distinct polarizations, defined by the phase matching conditions. However, by taking advantage of the phase matching conditions and detecting a coherent signal beam with orthogonal polarization in the probe propagation direction we restrict our observation purely to PS. We similarly aim to restrict our theoretical treatment to only those interactions in the sample that give rise to this specific signal beam.

We have performed experiments with low pulse energies that correspond to the weak field, perturbative limit. In this publication, we correspondingly treat the problem theoretically in the perturbative limit, using a diagrammatic approach and angular momentum tensor theory. Williams *et al.*[24,25] have described a diagrammatic spherical tensor treatment of DFWM in the weak field limit, and Wasserman *et al.*[26,27] have extended this to include initial ground state orientation and alignment, such as can arise from photodissociation or reaction. These authors made several assumptions that are not valid in the experiments described in this paper. As noted by Williams *et al.*,[24] these monochromatic frequency domain models for incident and generated fields necessarily demand that the population relaxation and collisional dephasing times must be much shorter than the temporal duration (nominally infinite) of the laser pulse. In subsequent finite bandwidth treatments[11,28] essentially the same formalism has been applied in situations where the pulse durations are much shorter than the decay rates. The functional forms derived in these treatments consisted of the sum over all interacting levels of a numerator, containing a fourfold transition matrix element, and a denominator, containing the resonant frequency and collisional dependence of the signal. The separation of the numerator and denominator was achieved by assuming that the relaxation and dephasing rates were independent of the m_J sublevel. The numerator could then be evaluated using the spherical tensor treatment. The result is a separation of the geometrical factors introduced by

the different photon polarizations from the dynamical contributions arising from population, orientation and alignment of the sample. Phenomenological decay rates for these parameters were then introduced to the resonant denominator. However, the experiments described in this paper are performed as a function of pump–probe delay rather than in the frequency domain and measure decays on a time scale significantly longer than the laser pulsewidth. The measurement of true orientation or alignment moments rather than phenomenological decay rates is their primary purpose. The main development that we describe here is a tensor moment approach to pump–probe PS measurements that isolates true orientation and alignment decay rates.

The diagrammatic approach to nonlinear optical calculations greatly simplifies the calculation of the polarization density matrix responsible for the generation of the third order nonlinear signal.[29–31] The complete density matrix can be broken down into individual contributions from each possible time-ordered sequence of photon interactions, represented by a double-sided Feynman diagram. At each interaction time, t_n, the quantum states participating are represented above and below the interaction point. Between the interaction times $t_1<t_2<t_3<t$, corresponding to the three photon interactions that generate the final signal wave at time, t, we have the respective delays τ_1, τ_2, and τ_3. During these delays, the system evolves field free. Any relaxation during these delays is the property of the system that we are interested in measuring.

Inspection of the diagrams shows clearly which interaction sequences contribute to the measured signal, and the relevant density matrix can then be calculated. When only two isolated J states are involved, one in the ground electronic state and one in the excited electronic state, and only the ground state has initial population, it is readily shown that only eight diagrams can contribute to the signal. These relevant diagrams are shown in Fig. 1, and can be broken down into two groups. The first group of four, labeled ''pump–probe,'' involve two interactions with the pump laser, followed by the probe. These diagrams represent the only processes that generate the signal when the probe pulse is significantly later than the pump pulse. The second four, labeled ''coherent,'' are those where the probe interacts with the sample laser either before, or in between, the pump interactions. When the probe pulse is well before the pump pulse only two of these diagrams will contribute to the signal, whereas all four will be significant when the pump and probe pulses overlap. The ''pump–probe'' diagrams also contribute when the pump and probe pulses are coincident, and hence all eight of the diagrams are important in this situation.

The Feynman diagrams may be used to direct the calculation of the signal electric field generated by each of the possible time-ordered sequences of interactions in the sample. Because the temporal evolution of the electric field strength of our ns-pulsed lasers is much slower than the optical cycle frequency, the resulting signal intensity that is detected experimentally will be a cycle average of the square modulus of the signal electric field strength.

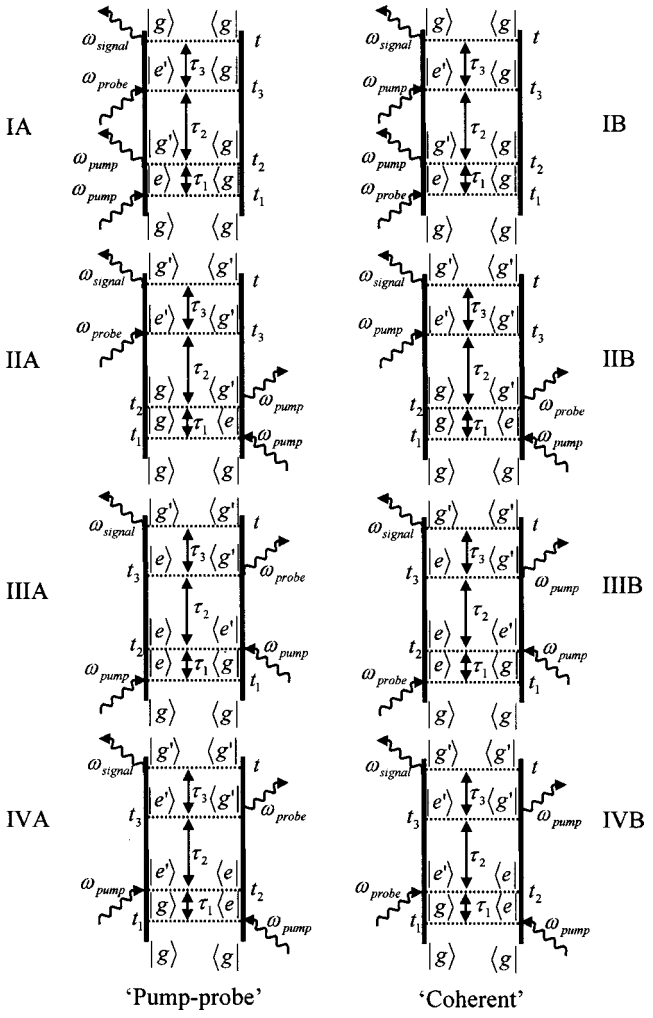

FIG. 1. Feynman diagrams for the eight possible time-ordered sequences of photon interactions giving rise to PS signals. First column, ''pump–probe'' diagrams IA–IVA, second column, ''coherent'' diagrams IB–IVB.

B. Perturbative derivation

The detailed derivation of the signal field contribution from diagram IA is given in the Appendix: here we discuss the key features only. The measured signals are integrals over the temporal characteristics of the experiment, principally the pulsewidths of the pump and probe lasers. The relaxation time scales and laser pulsewidths may be of similar magnitude in our experiments, precluding any simplification of the integrals. The integration over the laser pulsewidths is in general not a straightforward analytical task, even if we were to assume an idealized functional form to represent the complicated, not well defined, experimental laser pulse profiles.

Instead, we evaluate the signal field for specific, unique times and numerically integrate the results over suitable experimental parameters for the laser pulsewidths and detection gate in a Monte Carlo fashion, a procedure discussed in Sec. III. The calculation proceeds from an initially isotropic (and hence diagonal) ground state density matrix. We assume that at some time t_1 it undergoes an interaction with the first photon. The resulting density matrix can be found by application of the dipole operator. The result will be a linear su-

perposition of the ground and excited states, oscillating at the transition frequency. With the aid of the Wigner–Eckart theorem the result can be rearranged and expressed in terms of an expansion in state multipoles and spherical tensors.[32] Provided the medium is isotropic, which is the case for our experiments, the characterization of the relaxation of the state multipoles that describe the expansion will be straightforward.[33] All projections, Q, of a state multipole will relax at the same rate, but different ranks, K, will have different rates. The density matrix after this first interaction is described by a single multipole of rank $K=1$, representing coherence between the ground and excited states, or oscillating dipolar bulk polarization. The relaxation of this multipole during the time interval $\tau_1=t_2-t_1$ is determined by a single dephasing rate, Γ_d.

At this point, the density matrix can be expanded once more in terms of the state operators, the second photon interaction is applied and the same procedure repeated. This time, after some angular momentum manipulation, we find that the density matrix spans only the ground state, or only the excited state, depending on which diagram is considered. This corresponds physically to time-invariant, m_J-dependent population transfer from the ground to excited states. The hole burned in the ground state m_J distribution mirrors the populations created in the excited state. The density matrix may be defined in terms of tensors of rank $K=0$, 1, and 2. These are population, orientation and alignment tensors, respectively. Their evolution is the target of the experiments, and is discussed in detail in Sec. II C. They evolve with differing rates, Γ_{K_2}, during the period $\tau_2=t_3-t_2$. This period may be long if the pump and probe pulses are widely separated in time, as is possible with independent laser systems.

The third photon interaction is then applied in a similar fashion, giving a density matrix that relaxes with rate Γ_{K_3}, once again describing a superposition of the ground and excited states. The signal field associated with this third-order density matrix may be found by calculating the trace of the product of the density matrix with the dipole operator. Some straightforward angular momentum algebra shows that $K_3=1$ only, and consequently the relaxation rate Γ_{K_3} during the time $\tau_3=t-t_3$ is the same as Γ_d during time τ_1.

Similar calculations may be made for all eight diagrams, and it is found that the signal electric field generated by all of the diagrams can be described in a simple fashion. The diagrams forming ground state orientation and alignments (IA, IIA, IB, IIB) produce

$$\mathbf{P}^{(3)}(t)\cdot\boldsymbol{\varepsilon}_4^*=C\Phi e^{-\Gamma_d(\tau_1+\tau_3)}\sum_{K_2}\begin{Bmatrix}1 & J_g & J_e\\ J_g & 1 & K_2\end{Bmatrix}^2 \times F(\boldsymbol{\varepsilon}_1\boldsymbol{\varepsilon}_2\boldsymbol{\varepsilon}_3\boldsymbol{\varepsilon}_4;K_2)e^{-\Gamma_{K_2}^{J_g}\tau_2}. \quad (1)$$

Those diagrams forming excited state orientation and alignments (IIIA, IVA, IIIB, IVB) result in

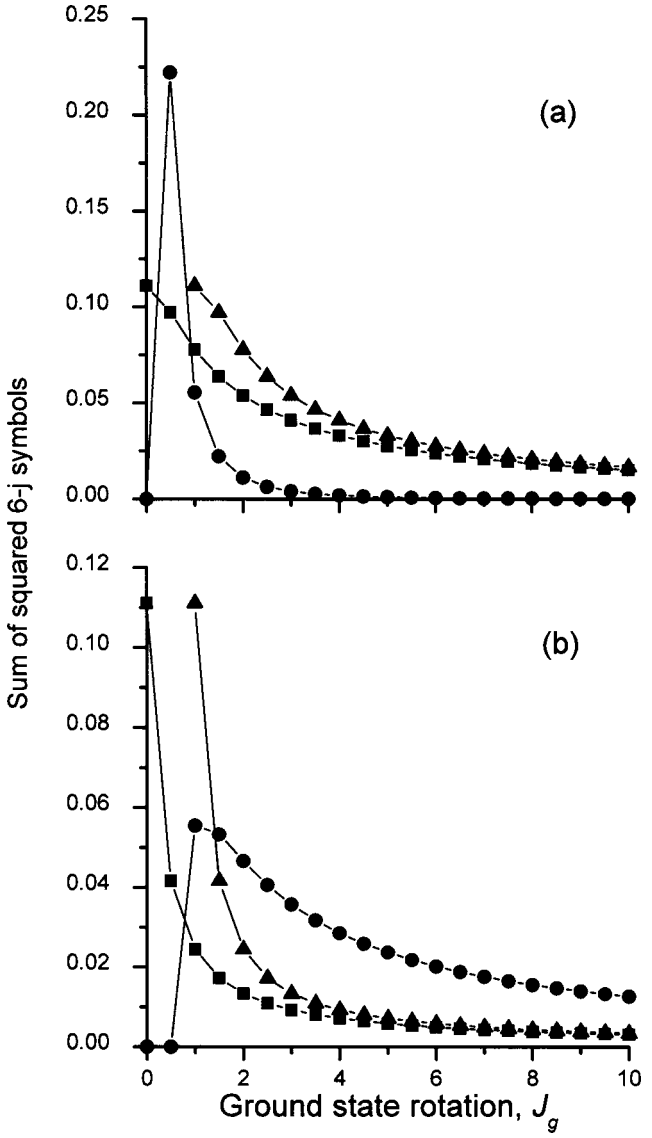

FIG. 2. (a) Orientation, $K=1$, dependence of sum of squared 6-j symbols from Eqs. (1) and (2) as a function of ground state rotational quantum number J_g in half-integer increments. Filled triangles, P branch; filled circles, Q branch; and filled squares, R branch. (b) Alignment, $K=2$, dependence, symbols as for (a).

$$\mathbf{P}^{(3)}(t)\cdot\boldsymbol{\varepsilon}_4^*=C\Phi e^{-\Gamma_d(\tau_1+\tau_3)}\sum_{K_2}\begin{Bmatrix}1 & J_e & J_g\\ J_e & 1 & K_2\end{Bmatrix}^2 \times F(\boldsymbol{\varepsilon}_1\boldsymbol{\varepsilon}_2\boldsymbol{\varepsilon}_3\boldsymbol{\varepsilon}_4;K_2)e^{-\Gamma_{K_2}^{J_e}\tau_2}. \quad (2)$$

These equations have a clear physical meaning. The first term, C, contains the dependence of the signal field on the number of molecules present, N, and the magnitudes of the three incident electric fields, ξ_n. It also depends on the reduced matrix element carrying the transition line strength,

$$C=\frac{N\xi_1\xi_2\xi_3|\langle J_e\|(\mu)^{(1)}\|J_g\rangle|^4}{8i\hbar^3(2J_g+1)}. \quad (3)$$

A coherent term, Φ, defines the phase-matching resulting from the time-ordered sequence of events and the field-free evolution of the system. The expression that holds for cases I and III is

TABLE I. Polarization factors $F(\varepsilon_1\varepsilon_2\varepsilon_3\varepsilon_4;K_2)$ for different tensor ranks K_2 and both left-hand circular and 45° linear pump polarizations. Values for right-hand circular pump polarization are the same as for left circular other than a change of sign for $K_2=1$.

	Left circular pump polarization			Linear pump polarization		
Diagram	$K_2=0$	$K_2=1$	$K_2=2$	$K_2=0$	$K_2=1$	$K_2=2$
IA	0	$i/2$	0	0	0	1/2
IIA	0	$i/2$	0	0	0	1/2
IIIA	0	$i/2$	0	0	0	1/2
IVA	0	$i/2$	0	0	0	1/2
IB	$i/6$	$i/4$	$-5i/12$	1/6	−1/4	1/12
IIB	$i/6$	$i/4$	$-5i/12$	1/6	−1/4	1/12
IIIB	$i/6$	$i/4$	$-5i/12$	1/6	−1/4	1/12
IVB	$i/6$	$i/4$	$-5i/12$	1/6	−1/4	1/12

$$\Phi = e^{-i\omega_s t + i\mathbf{k}_s\cdot\mathbf{r}} e^{i\tau_3(\omega_s-\omega_{J_eJ_g})} e^{i\tau_2(\omega_1-\omega_2)} e^{i\tau_1(\omega_1-\omega_{J_eJ_g})}. \tag{4}$$

The signal frequency $\omega_s=\omega_1-\omega_2+\omega_3$, with ω_1 and ω_2 from the pump laser and ω_3 from the probe laser for cases IA and IIIA. For cases IB and IIIB we must swap the sources of ω_1 and ω_3, so that the probe photon comes first. The wave vector defines the propagation direction of the signal beam, $\mathbf{k}_s=\mathbf{k}_1-\mathbf{k}_2+\mathbf{k}_3$. The functional form of Φ for cases II and IV is slightly different, namely,

$$\Phi = e^{-i\omega_s t + i\mathbf{k}_s\cdot\mathbf{r}} e^{i\tau_3(\omega_s-\omega_{J_eJ_g})} e^{i\tau_2(\omega_2-\omega_1)} e^{i\tau_1(\omega_{J_eJ_g}-\omega_1)}. \tag{5}$$

Now $\omega_s=\omega_2-\omega_1+\omega_3$ with ω_1 and ω_2 from the pump laser and ω_3 from the probe for the ''pump–probe,'' case IIA and IVA, whilst for the ''coherent'' case IIB and IVB we must swap ω_2 and ω_3 so that the probe photon comes second. This time the wave vector is given by $\mathbf{k}_s=\mathbf{k}_2-\mathbf{k}_1+\mathbf{k}_3$.

All of the cases are affected equally by the dephasing rate, Γ_d, during the combined times $\tau_1+\tau_3$. The population, orientation and alignment sensitivity is contained in the sum over K_2, which is restricted to $K_2=0$, 1 or 2. The 6-j symbol in Eqs. (1) and (2) reflects the transition sensitivity to these different moments, depending on whether the moment describes a population, orientation, or alignment in the ground or excited state. The total signal electric field will result from the sum of the fields contributed by the different diagrams. To illustrate the tensor moment dependence of the signal electric field on different transitions we evaluate the sum of the squared 6-j symbols appearing in Eqs. (1) and (2). Figure 2(a) shows the results for the orientation dependence, $K_2=1$, and Fig. 2(b) for the alignment dependence, $K_2=2$. The sum is shown for *P*, *Q*, and *R* branch transitions, as a function of the ground state rotational quantum number, J_g, in half-integer steps. Strong dependencies on rotational branch and quantum number are seen. Figure 2(a) shows the expected rapid decrease in orientation sensitivity via *Q* branch transitions with increasing J_g, together with a more gradual decline in *P* and *R* branch sensitivity tending towards a constant value at high J_g. Figure 2(b) shows that alignment sensitivity is higher on the *Q* branches at all except the lowest J_g, with the *P* and *R* branch sensitivity declining to one quarter of the *Q* branch sensitivity at high J_g. A minimum of two m_J substates in either the ground or excited levels is required for orientation, and a minimum of three is required for alignment. Hence, for example, alignment signal cannot be generated on a $Q(0.5)$ transition, as both ground and excited states only possess two m_J substates.

The final term $F(\boldsymbol{\varepsilon}_1\boldsymbol{\varepsilon}_2\boldsymbol{\varepsilon}_3\boldsymbol{\varepsilon}_4;K_2)$ in Eqs. (1) and (2) contains the geometrical dependence of the signal on the polarizations of the pump, probe, and signal photons. For cases I and III this has the form

$$\begin{aligned} F(\boldsymbol{\varepsilon}_1\boldsymbol{\varepsilon}_2\boldsymbol{\varepsilon}_3\boldsymbol{\varepsilon}_4;K_2) = \sum_{Q_1,Q_2,Q_3} & (-1)^{Q_2}(2K_2+1)(\varepsilon_1)^{(1)}_{-Q_1} \\ & \times(\varepsilon_2^*)^{(1)}_{Q_1-Q_2}(\varepsilon_3)^{(1)}_{Q_2-Q_3}(\varepsilon_4^*)^{(1)}_{Q_3} \\ & \times\begin{pmatrix} 1 & 1 & K_2 \\ Q_2-Q_1 & Q_1 & -Q_2 \end{pmatrix} \\ & \times\begin{pmatrix} 1 & 1 & K_2 \\ Q_2-Q_3 & Q_3 & -Q_2 \end{pmatrix} \end{aligned} \tag{6}$$

and for cases II and IV the result is

$$\begin{aligned} F(\boldsymbol{\varepsilon}_1\boldsymbol{\varepsilon}_2\boldsymbol{\varepsilon}_3\boldsymbol{\varepsilon}_4;K_2) = \sum_{Q_1,Q_2,Q_3} & (-1)^{K_2+Q_2}(2K_2+1) \\ & \times(\varepsilon_1^*)^{(1)}_{-Q_1}(\varepsilon_2)^{(1)}_{Q_1-Q_2}(\varepsilon_3)^{(1)}_{Q_2-Q_3} \\ & \times(\varepsilon_4^*)^{(1)}_{Q_3}\times\begin{pmatrix} 1 & 1 & K_2 \\ Q_2-Q_1 & Q_1 & -Q_2 \end{pmatrix} \\ & \times\begin{pmatrix} 1 & 1 & K_2 \\ Q_2-Q_3 & Q_3 & -Q_2 \end{pmatrix}. \end{aligned} \tag{7}$$

The experimental geometries used in polarization spectroscopy define the probe and signal beams to have orthogonal linear polarizations. The pump photons must, by definition, both have the same polarization, which is either circular, or linear (normally at 45° to the probe polarization, maximizing the signal) at the choice of the experimenter. Using these polarizations in the different cases to define ε_n, and the relevant Eqs. (6) or (7), the $F(\boldsymbol{\varepsilon}_1\boldsymbol{\varepsilon}_2\boldsymbol{\varepsilon}_3\boldsymbol{\varepsilon}_4;K_2)$ can be found and are listed in Table I. The ''pump–probe'' diagrams IA–IVA are found, as might intuitively be expected, to be dependent on a single tensor moment only, either $K_2=1$ (orientation) if the pump photons are circular, or $K_2=2$ (alignment) if the pump photons are linear. Crucially, the evolution of the signal when the pump and probe lasers are well separated in time, when only these diagrams contribute, will therefore enable the relaxation of a single tensor moment to be studied.

C. Orientation and alignment moments

The previous section showed how the signal is dependent on the K_2 tensor moments, which we have described as orientation or alignment in the ground or excited states. Consider the density matrix immediately after two interactions, $\rho^{(2)}(t_2)$, for diagram IA [Eq. (A13)]. Collecting the complex phase-dependent part and the square of the reduced matrix element into a constant *D* this can be written

TABLE II. Alignment moments for Feynman diagrams IA or IIA in Fig. 1, after interaction with two pump photons. The upper signs apply for left circular polarization and the lower for right circular. (a) *P* branch, (b) *Q* branch and (c) *R* branch.

Alignment moment	Circular pump	Linear pump
(a)		
$A_0^{(0)}(J_g)$	1	1
$A_0^{(1)}(J_g)$	$\mp\frac{1}{2\sqrt{3}}\left[\frac{J_g+1}{J_g}\right]^{1/2}$	0
$A_0^{(2)}(J_g)$	$\frac{1}{10}\left[\frac{2J_g+3}{J_g}\right]$	$\frac{1}{10}\left[\frac{2J_g+3}{J_g}\right]$
$A_{2-}^{(2)}(J_g)$	0	$\frac{\sqrt{3}}{10}\left[\frac{2J_g+3}{J_g}\right]$
(b)		
$A_0^{(0)}(J_g)$	1	1
$A_0^{(1)}(J_g)$	$\mp\frac{1}{2\sqrt{3}}\left[\frac{1}{J_g(J_g+1)}\right]^{1/2}$	0
$A_0^{(2)}(J_g)$	$-\frac{1}{10}\left[\frac{(2J_g-1)(2J_g+3)}{J_g(J_g+1)}\right]$	$-\frac{1}{10}\left[\frac{(2J_g-1)(2J_g+3)}{J_g(J_g+1)}\right]$
$A_{2-}^{(2)}(J_g)$	0	$\frac{\sqrt{3}}{10}\left[\frac{(2J_g-1)(2J_g+3)}{J_g(J_g+1)}\right]$
(c)		
$A_0^{(0)}(J_g)$	1	1
$A_0^{(1)}(J_g)$	$\pm\frac{1}{2\sqrt{3}}\left[\frac{J_g+1}{J_g}\right]^{1/2}$	0
$A_0^{(2)}(J_g)$	$\frac{1}{10}\left[\frac{2J_g-1}{J_g+1}\right]$	$\frac{1}{10}\left[\frac{2J_g-1}{J_g+1}\right]$
$A_{2-}^{(2)}(J_g)$	0	$\frac{\sqrt{3}}{10}\left[\frac{2J_g-1}{J_g+1}\right]$

$$\rho^{(2)}(t_2)=D\sum_{K_2,Q_1,Q_2}(-1)^{K_2+J_g+J_e}(\varepsilon_1)^{(1)}_{-Q_1}(\varepsilon_2^*)^{(1)}_{Q_1-Q_2}\times(2K_2+1)^{1/2}\begin{Bmatrix}1 & J_g & J_e\\ J_g & 1 & K_2\end{Bmatrix}\times\begin{pmatrix}1 & 1 & K_2\\ Q_2-Q_1 & Q_1 & -Q_2\end{pmatrix}T^{K_2}_{Q_2}(J_gJ_g). \quad (8)$$

This can be expressed in terms of spherical tensor moments, and those moments related to the alignment moments as conventionally defined.[17] In this derivation, the alignment moments are referenced to a *Z*-axis parallel to the direction of propagation of the beams, regardless of whether circular or linear pump light is used. Table II lists, as an example, the renormalized alignment moments in this frame generated by diagrams IA or IIA in the ground state for *P*, *Q*, and *R* branches by a circular or 45° linear polarized pump beam.

This treatment shows that after two photons have interacted with the sample it consists of an oriented or aligned population in the ground state, and a complementary oriented or aligned population in the excited state. The subsequent polarization selection in the probe and detection steps constraints the sensitivity of PS to these moments further, as is apparent from Table I. However, this analysis makes it clear that the experiments are directly sensitive to the orientation and alignment of the rotational angular momentum of the ground and excited states, and their evolution.

The results described in Sec. II A above show that for Feynman diagram IA, only the decay of a single moment of the distribution is measured, dependent on the polarization of the pump light. It might be inferred that the population moment $K_2=0$ is seemingly not measured. However, clearly the signal must be sensitive to the population; as without a sample present no signal can be measured! The resolution of this apparent contradiction lies in recognizing that the relaxation rates for orientation and alignment as defined are total rates for the bulk loss of these properties, and include all processes that remove population from the *J* state, as well as the Δm_J changing events within that state.

D. Effect of Doppler motion

The preceding sections have treated all molecules in the sample as being at rest with respect to the beam propagation direction. In practice the distribution of velocities in the sample leads to different velocity subgroups ''seeing'' different fields, and hence forming different third order density matrices. This Doppler effect may be included in an established fashion.[30] We define the position of the molecule at time t as $\mathbf{r}(t)$. At an earlier time, t_n, the position was $\mathbf{r}(t_n)=\mathbf{r}(t)-(t-t_n)\mathbf{v}$, where $\mathbf{v}$ is the constant velocity of the molecule. For example, at time t_1 we can write the electric field incident in diagram IA as

$$E(t_1)=\xi_1\boldsymbol{\varepsilon}_1 e^{-i\omega_1 t_1+i\mathbf{k}_1\cdot\mathbf{r}(t)-i\mathbf{k}_1\cdot\mathbf{v}(\tau_3+\tau_2+\tau_1)}. \quad (9)$$

This Doppler effect can be applied to the incident electric fields at all three times, and results in changes to the phase-dependent term Φ in Eq. (1). The new Φ terms, assuming the pump photons are identical, are listed in Table III. The dot product **k.v** assures that only the projection of the velocity onto the wave vectors is important, as required physically. All of the wave vectors are assumed collinear in this treatment, and we need only consider the one-dimensional projection of the Maxwell–Boltzmann velocity distribution, which is a Gaussian distribution.

The thermal motion manifests itself through two effects. First, the lasers will come into resonance with molecular subgroups at frequencies away from the natural transition frequency. This gives rise to the expected Gaussian line broadening. Second, the presence of the **k.v** term during delays τ_1 and τ_3 results in the rapid loss of the signal. We illustrate this effect using the example of the OH radical. The OH $A-X$ (0,0) band is at $\approx$308 nm, giving $|\mathbf{k}|\approx 2\times10^7\ \mathrm{m}^{-1}$. The Gaussian one-dimensional velocity distribution has a half width at half maximum equal to 381 $\mathrm{m\,s}^{-1}$. A phase shift of 2π then arises between molecules with this velocity projection and those that have zero velocity projection in less than 1 ns. The Doppler motion of the molecules thus gives rise to a wide range of phase angles within a short delay time. The consequence of this is that the effective electric fields closely follow the temporal shapes of the laser pulses, i.e., no signal is seen at negative pump–probe delays, and no free induction decay is observed following the probe pulse. During τ_2 however, no dependence on the wave vector

TABLE III. Phase factors including the effect of Doppler motion, assuming pump photons are identical, for the different Feynman diagrams in Fig. 1.

IA and IIIA	$\Phi = e^{-i\omega_s t + i\mathbf{k}_s\cdot\mathbf{r}(t)} e^{i\tau_3(\omega_{\text{probe}} - \omega_{J_e J_g} - \mathbf{k}_{\text{probe}}\cdot\mathbf{v})} e^{i\tau_1(\omega_{\text{pump}} - \omega_{J_e J_g} - \mathbf{k}_{\text{pump}}\cdot\mathbf{v})}$
IIA and IVA	$\Phi = e^{-i\omega_s t + i\mathbf{k}_s\cdot\mathbf{r}(t)} e^{i\tau_3(\omega_{\text{probe}} - \omega_{J_e J_g} - \mathbf{k}_{\text{probe}}\cdot\mathbf{v})} e^{i\tau_1(\omega_{J_e J_g} - \omega_{\text{pump}} + \mathbf{k}_{\text{pump}}\cdot\mathbf{v})}$
IB and IIIB	$\Phi = e^{-i\omega_s t + i\mathbf{k}_s\cdot\mathbf{r}(t)} e^{i\tau_3(\omega_{\text{probe}} - \omega_{J_e J_g} - \mathbf{k}_{\text{probe}}\cdot\mathbf{v})} e^{i\tau_2(\omega_{\text{probe}} - \omega_{\text{pump}} + [\mathbf{k}_{\text{pump}} - \mathbf{k}_{\text{probe}}]\cdot\mathbf{v})} e^{i\tau_1(\omega_{\text{probe}} - \omega_{J_e J_g} - \mathbf{k}_{\text{probe}}\cdot\mathbf{v})}$
IIB and IVB	$\Phi = e^{-i\omega_s t + i\mathbf{k}_s\cdot\mathbf{r}(t)} e^{i\tau_3(\omega_{\text{probe}} - \omega_{J_e J_g} - \mathbf{k}_{\text{probe}}\cdot\mathbf{v})} e^{i\tau_2(\omega_{\text{probe}} - \omega_{\text{pump}} + [\mathbf{k}_{\text{pump}} - \mathbf{k}_{\text{probe}}]\cdot\mathbf{v})} e^{i\tau_1(\omega_{J_e J_g} - \omega_{\text{pump}} - \mathbf{k}_{\text{pump}}\cdot\mathbf{v})}$

is seen in Table III. Physically there is no spatial variation in the population, orientation or alignment created. This is in contrast to the spatially varying gratings generated in general case of FWM experiments with noncollinear beams.[24]

E. Velocity-changing collisions

The previous section described how the velocity distribution of the detected species was important in the evolution of the PS signal. Clearly then, changes in the velocity distribution during the overall pumping and probing process may be expected to have a significant effect on the signal. As far as we are aware, however, velocity-changing collisions have not been considered in the interpretation of any of the previous published studies of PS. However, there have been a number of publications on their effect on other third order nonlinear spectroscopic techniques, notably photon echo spectroscopies.[34–36] One approach to the inclusion of velocity-changing collisions is to introduce a collision kernel that gives the probability density per unit time that a collision changes the velocity from $\mathbf{v}$ to $\mathbf{v}'$. In principle, this kernel can have almost any form, determined by the dynamics of the interaction between molecule and collision partner. We will therefore make some assumptions to simplify the problem for illustrative purposes. It will be assumed that the time scale of the collisions is negligible compared to the time scale of the laser pulses. This impact approximation should be valid for ns-pulsed lasers and ps collision time scales. It will further be assumed that the collisions are hard, such that the velocity distribution is completely thermalized after a single collision. Finally, we assume that there is no correlation between rotational angular momentum polarization and velocity-changing collision cross sections.

We will consider velocity-changing collisions in two different time regimes. The first is during delay periods τ_1 and τ_3, when the system is in a coherent superposition of ground and excited states. If the collisional interaction is different for the two states, which will be the case in general, then the collision kernel is no longer constrained to be positive definite, but may be complex.[37] The effect of the collisions, considering only the real part of the collision kernel, can be seen by inspecting the relevant premultipliers in Table III. During delays τ_1 and τ_3 the premultiplier depends on the velocity projection along the laser propagation direction. Changing this velocity will result in a loss of signal, in a precisely analogous fashion to the effect of the Doppler motion described in Sec. II D. To illustrate this, consider two molecules initially having the same velocity and same position. Without any collisions, the molecules will stay exactly in phase, interacting identically until finally generating in-phase contributions to the signal beam at time *t*. If instead, one of the molecules undergoes a velocity-changing collision during τ_1, then it will be at a different point in space to the other molecule when it interacts with the second photon. This dephasing destroys the PS signal. The same phenomenon occurs during τ_3. Both of these processes are operating during delay periods defined by the respective pump and probe laser pulse-lengths. In an experiment where the pump–probe delay is varied, they will reduce the absolute signal size by a fixed proportion, but will not cause decay as a function of the pump–probe delay. In our previous experiments where the pressure of collider gas was varied at a fixed, coincident pump-probe delay we saw extremely rapid decay of the PS signal.[16] We have attributed this predominately to the effect of these velocity-changing collisions.

We now consider collisions that occur during delay τ_2. In Table III we see that the premultiplier is not sensitive to this delay at all, assuming that the pump photons are identical. Yet clearly if the molecule undergoes a collision during this delay period, the velocity during τ_3 will be different from that during τ_1. What effect is expected from these collisions? There is a straightforward physical interpretation. That portion of the Doppler profile that was in resonance with the pump laser has been preferentially excited, with a velocity width determined in practice by the bandwidth of the laser. If we assume the probe laser has the same frequency as the pump laser then any collisions during τ_2 that change the velocity tend to move the sample out of resonance with the probe laser. This will clearly result in a decrease in the observed signal. With single mode lasers, only a small fraction of the Doppler profile would be pumped and probed at any laser center frequency. In that case, velocity-changing collisions during this delay period would have a significant impact on the dependence of the signal on the pump–probe delay. When using typical commercial ns-pulsed dye lasers, however, the relatively broad spectral output of the lasers will result in a significant fraction of the Doppler profile being in resonance. In this case, these velocity-changing collisions will be less important.

We thus expect that the principal effect of velocity-changing collisions on the observed PS signals using commercial ns-pulsed lasers will be the reduction in absolute magnitude of the signal, resulting from the dephasing influence of collisions during delays τ_1 and τ_3. We expect the evolution of the signal as a function of pump–probe delay to be dominated by collisional loss of population, orientation or alignment, rather than by the modest effect of velocity-changing collisions.

F. Nuclear hyperfine depolarization

Optical excitation in these small radicals creates orientation and alignment of the angular momentum, **J**, the result of the coupling of the nuclear rotational and electronic spin and orbital angular momenta. However, **J** may also be coupled to the nuclear spin of the molecule. This effect has been described in the study of angular momentum alignment resulting from photodissociation, reaction or optical pumping.[17,32,33] Although the influence of nuclear hyperfine depolarization has been studied in FWM (Refs. 38–40) and used to perform quantum beat spectroscopy, there has been no explicit discussion of hyperfine interactions in PS. We will simplify the problem by only considering the nuclear hyperfine coupling during the delay period τ_2. This is justified on the following grounds. First, this is the only delay period under our direct control, such that we may expect to be able to probe any hyperfine effects as a modulation in the observed signal. Second, the time scale of the nuclear hyperfine coupling effects is determined by the strength of the coupling between the nuclear spin **I** and angular momentum **J**. If the different resultant states **F** from this coupling are to be excited by the same laser pulse, then this coupling cannot occur on a timescale much faster than the laser pulse. We do not therefore expect significant nuclear hyperfine depolarization during the time scale of the laser pulse, and hence τ_1 and τ_3.

Making these assumptions, and recognizing that the system during the delay τ_2 may be described by an expansion in orientation and alignment spherical tensors, we may use the procedure described in the literature.[32,33] The depolarization of **J** can be described in the vector model in the following fashion. **J** and the nuclear spin **I** couple to give **F**. **J** then precesses about **F** so that the prepared direction of **J** in the space-fixed frame is altered. When **I** is of a similar magnitude to **J** the depolarization will be significant. When **J** is large then **F** and **J** will be nearly parallel and the depolarization will be small. The depolarization will display a periodic nature, with **J** occasionally returning to its initial prepared direction. For a single nuclear spin **I** coupling to **J** it may be shown[32] that the depolarization affects all spherical tensor components of rank K equally, such that the time dependence of a spherical tensor may be expressed as

$$\rho_Q^K(t)=\rho_Q^K(t=0)G^K(t), \tag{10}$$

where the depolarization factor $G^K(t)$ is given by

$$G^K(t)=\sum_{F,F'}\frac{(2F+1)(2F'+1)}{(2I+1)}\begin{Bmatrix} F' & F & K \\ J & J & I \end{Bmatrix}^2 \times\cos\left[\frac{(E_{F'}-E_F)t}{\hbar}\right]. \tag{11}$$

The hyperfine nuclear depolarization is thus shown to be oscillatory in nature, with periods defined by the energy splittings, $E_{F'}-E_F$, between the different nuclear hyperfine states. The magnitude of the effect is determined by the 6-j symbol, ensuring that it is negligible when $J\gg I$. In the simulations described in Sec. III, we explore the effect of nuclear hyperfine depolarization on PS signals for the OH $A\,^2\Sigma^+-X\,^2\Pi$ transition.

III. SIMULATION OF PS SIGNALS

A. Simulation procedure

The preceding sections have detailed an approach to the simulation of one-color PS signals. To simulate any experimental signals we need to integrate the equations describing the generated signal field over the full range of possible times, t_n, defined by the laser pulsewidths and the signal detection time, t, defined by the timegate over which detectable signal is generated. This integration has been performed numerically using a Monte Carlo (MC) approach, which we now describe.

Three separate times, t_n, are MC selected from the two laser pulsewidths; two from the pump pulse and one from the probe pulse, both of which are modeled as Gaussian distributions. The pump pulse is assumed to be centered at time zero, and the probe pulse center time is stepped over the desired range to reproduce that in the experiment; typically -20 to $+100$ ns. The pulsewidths are chosen to best reflect the measured values of the experimental laser pulses. A fourth time, t, is chosen as the detection time. This is MC selected from a uniform distribution, which starts at the latest of the three previously selected times and typically extends for 5–10 ns. This represents a compromise between computational efficiency and simulation of the boxcar gate in the experimental detection system. A target molecule velocity along the laser propagation axis is MC selected from the Gaussian distribution that is the one-dimensional projection of the Maxwell–Boltzmann velocity distribution for that temperature.

The time ordering of the two pump and one probe photons selected is now used to find which of the eight Feynman diagrams IA–IVB are relevant. For example, when the probe photon is the latest all four of the ''pump–probe'' diagrams, IA–IVA, contribute to the signal. The signal field that is generated from these diagrams is then calculated using the four selected times, using Eqs. (1)–(7). The effect of Doppler motion is introduced using the selected velocity. The collisional evolution of the signal is included by selected collisional relaxation rates Γ_d and Γ_{K_2}. The effect of hyperfine nuclear depolarization through the delay period τ_2 is included using Eq. (11). The signal fields generated by each diagram are summed, for a large number, typically $>10^6$, of iterations of this procedure. The total signal field generated is the sum of the contributions of the individual diagrams. The resulting signal intensity is the product of this signal field and its complex conjugate. This simulates the signal intensity for a particular chosen delay between the pump and probe pulsewidth centers. The probe pulse center time is then moved and the process repeated. Software to simulate the PS signals was written in FORTRAN, and the simulations performed on a PC workstation (dual 2.8 GHz Intel Xeon).

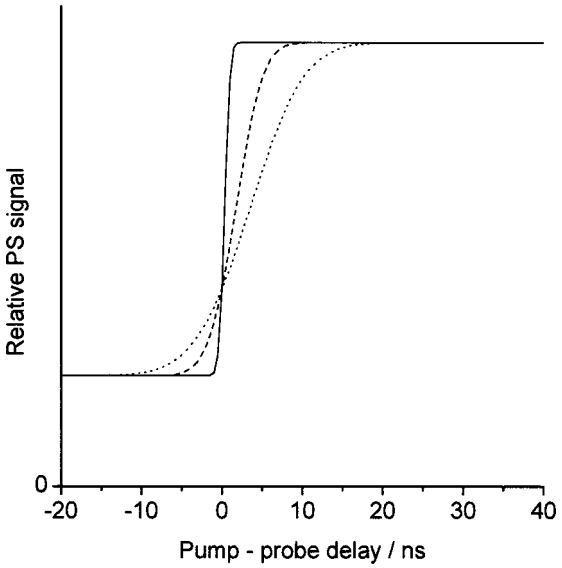

FIG. 3. Simulation of PS of OH $A\,^2\Sigma^+ - X\,^2\Pi$ (0,0) $Q_1(2.5)$ as a function of pump–probe delay for different, assumed equal, pump and probe laser pulsewidths. Simulations assumed no decay processes and a translational temperature of 1×10^{-8} K. Solid line, 1 ns pulsewidths; dashed line, 5 ns; dotted line, 10 ns.

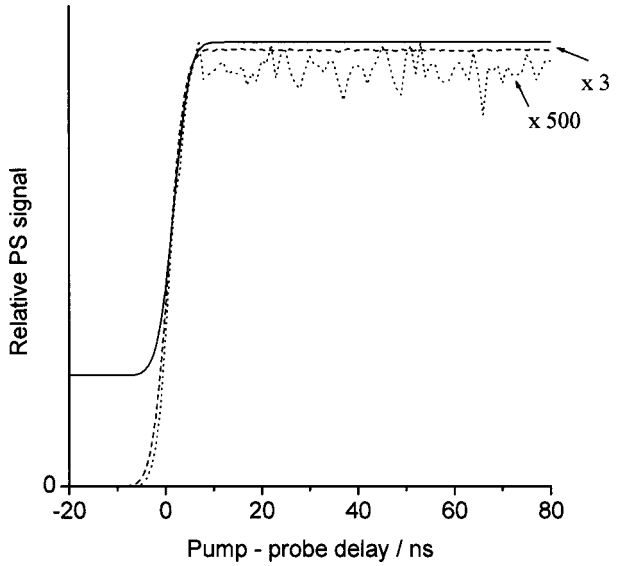

FIG. 4. Simulation of PS of OH $A\,^2\Sigma^+ - X\,^2\Pi$ (0,0) $Q_1(2.5)$ as a function of pump–probe delay for different translational temperatures. Simulations assumed no collisional decay processes and laser pulsewidths of 5 ns for both pump and probe. Solid line, 1×10^{-8} K; dashed line, 1 K intensity scaled by a factor of 3; dotted line, 298 K scaled by a factor of 500.

B. Illustrative simulations

Simulations were performed for illustrative purposes on the $Q_1(2.5)$ transition of the OH $A\,^2\Sigma^+ - X\,^2\Pi(0,0)$ band, assuming linearly polarized pump light. Pump and probe lasers frequencies were centered at the transition frequency, and the lasers were assumed to have identical pulsewidths. In all the simulations, except that exploring the effect of velocity-changing collisions, the laser outputs were assumed to be of a single common central frequency. Typical ns-pulsed dye lasers do not produce a pure single mode output. It might be expected that using multimode lasers would produce a change in the absolute signal size, but no variation in the signal as a function of pump–probe delay. We have performed exploratory calculations on the effect of multimode lasers, and have indeed found no changes in the relative variation of the simulated signal with pump–probe delay. We therefore do not discuss further the effects of multimode lasers in this paper.

We first demonstrate the dependence of the PS signal on the pump–probe delay on the purely hypothetical assumptions that there are no decay processes operating, and that Doppler motion is insignificant (translational temperature 1×10^{-8} K). Figure 3 shows the resulting simulations for laser pulsewidths of 1, 5, and 10 ns. All three simulations show signal at negative pump–probe delays, which arises from the processes shown in Feynman diagrams IB and IIIB. The signal rises sharply at the pump firing time and then continues at a constant value determined by the four ''pump–probe'' Feynman diagrams. The risetime of the signal is clearly dependent on the pulsewidth. However, the signal peak is not centered at zero delay, but is instead displaced to positive pump–probe delay, increasing with pulsewidth. This is a result of the pump pulse building up oriented or aligned population in the ground and excited states, with the maximum being reached at the end of the pump pulse.

The simulations in Fig. 4 are the result of varying the translational temperature from 1×10^{-8} K through 1 K to 298 K, but maintaining the assumption of no other decay processes. Each of these simulations assumed a 5 ns pulsewidth and involved 1×10^6 MC iterations per pump–probe delay time step. Two temperature dependent effects stand out. First, both the 1 and 298 K simulations show effectively no signal before the pump pulse occurs. Second, the 1 K signal is approximately three times, and the 298 K signal approximately 500 times, smaller than the 1×10^{-8} K signal. Both of these effects are a result of the Doppler motion of the sample. The loss of the signal at negative pump–probe delays is the result of the velocity-induced dephasing process described in Sec. II C above. As the temperature increases, a smaller proportion of the velocity distribution is in resonance with the lasers, decreasing the signal size.

Figure 5 shows the effect of including the radiative decay of the excited state. This simulation assumes a 5 ns laser pulsewidth, 298 K thermal velocity distribution, and uses the LIFBASE (Ref. 41) total radiative rate for the $A\,^+\Sigma$ ($v=0, J=2.5, F_1$) level probed by the $Q_1(2.5)$ transition, $k_{\mathrm{rad}}=1.45\times10^6\ \mathrm{s}^{-1}$. The resulting simulation shows a decay due to the radiative process as signal resulting from the excited state is lost, followed at long delays by a constant signal from the remaining ground state. Note the large change of time scale from Figs. 3 and 4. This remnant signal is a quarter of the magnitude of the initial $\Delta t=0$ signal. The initial signal was determined by the four pump–probe diagrams, which for this transition and polarization each contribute the same amount to the overall signal electric field. At long times only two of these diagrams remain, IA and IIA. Consequently, the signal field is halved in strength and the signal intensity drops to a quarter of the initial value. This

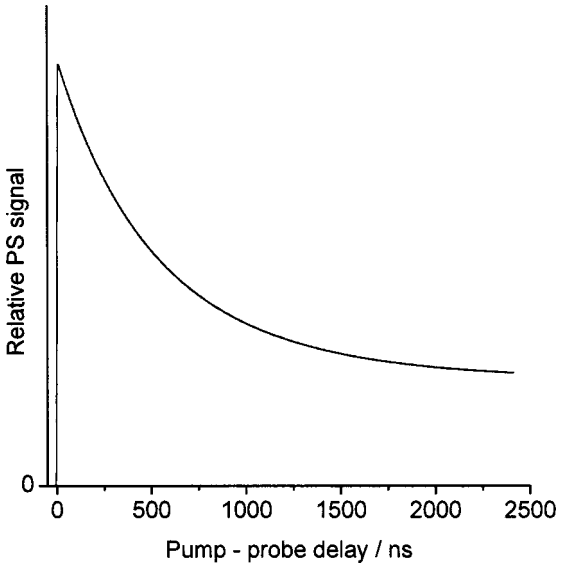

FIG. 5. Simulation of PS of OH $A\,^2\Sigma^+ - X\,^2\Pi$ (0,0) $Q_1(2.5)$ as a function of pump–probe delay showing effect of radiative decay, $k_{rad}=1.45\times10^6\ s^{-1}$, of the excited state. Simulations assumed pump and probe laser pulsewidths of 5 ns, no other collisional decay processes and a translational temperature of 298 K.

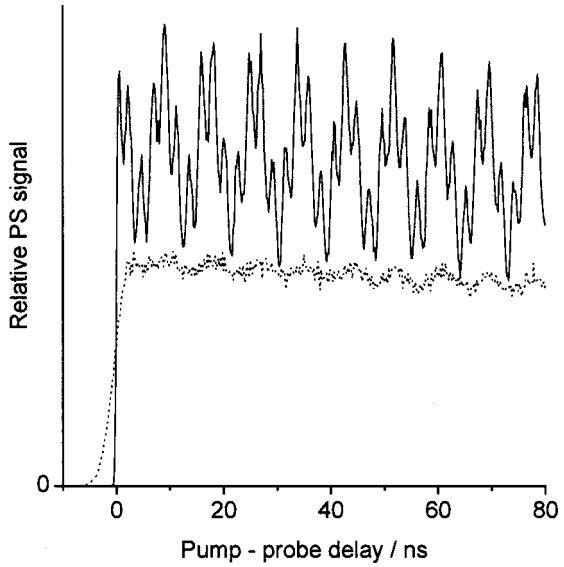

FIG. 7. Simulation of PS of OH $A\,^2\Sigma^+ - X\,^2\Pi$ (0,0) $Q_1(2.5)$ as a function of pump–probe delay showing the influence of nuclear hyperfine depolarization for different pump and probe laser pulsewidths. Simulations included radiative decay of $k_{rad}=1.45\times10^6\ s^{-1}$ but no collisional decay processes. The translation temperature was 298 K. Solid line, laser pulsewidth 0.5 ns; dashed line, laser pulsewidth 5 ns.

shows how the signal may not decay as a single exponential, as it depends on the sum of different exponential decays with possibly different weighting factors.

Figure 6 shows simulations with increasing collisional loss rates, introducing conditions more typical of those in experiments. The pulsewidths are again 5 ns, the temperature 298 K, the radiative decay rate is $k_{rad}=1.45\times10^6\ s^{-1}$, and the collider number density is $3.24\times10^{16}\ cm^{-3}$. The collisional rate constants for ground and excited states are assumed to be identical, and only the $K_2=2$ alignment rate constants are significant for this case of linear pump light. The decay rate constants are (a) $1\times10^{-10}\ cm^3\,s^{-1}$, (b) $5\times10^{-10}\ cm^3\,s^{-1}$, and (c) $1\times10^{-9}\ cm^3\,s^{-1}$. The resulting curves are essentially single exponential decays, with rates twice that implied by the rate constants. The single exponential nature of the decay is a consequence of using the same decay constants for ground and excited states. These curves show that at the typical pressures, of order 1 Torr, used in our own collisional energy transfer studies, and physically reasonable collisional decay constants, the PS signal is expected to disappear for pump–probe delays of the order of 100 ns.

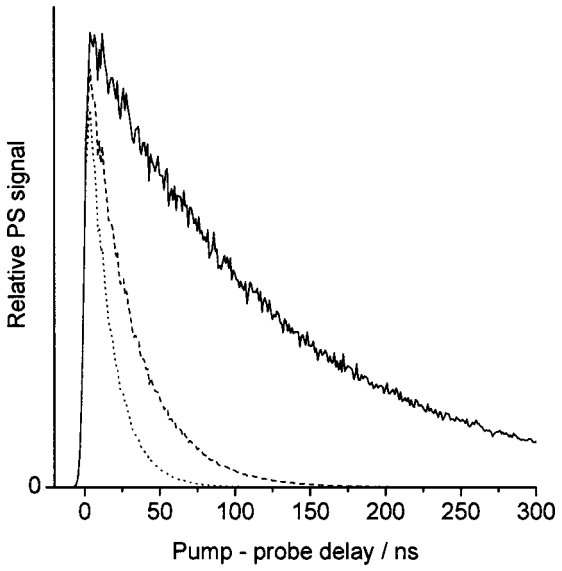

FIG. 6. Simulation of PS of OH $A\,^2\Sigma^+ - X\,^2\Pi$ (0,0) $Q_1(2.5)$ as a function of pump–probe delay for different collisional decay rate constants at a number density of $3.24\times10^{16}\ cm^{-3}$. Simulations assumed pump and probe laser pulsewidths of 5 ns, a radiative decay rate $k_{rad}=1.45\times10^6\ s^{-1}$, and a translational temperature of 298 K. Collisional rate constants were identical for ground and excited states. Solid line, $1\times10^{-10}\ cm^3\,s^{-1}$; dashed line, $5\times10^{-10}\ cm^3\,s^{-1}$; dotted line, $1\times10^{-9}\ cm^3\,s^{-1}$.

Nuclear hyperfine depolarization effects are introduced in Fig. 7. In the simulation shown by the solid line, the laser pulsewidths are reduced to 0.5 ns, the time step to 0.2 ns, and 2×10^6 iterations of the MC procedure were calculated at each time step. Collisional relaxation processes have not been included, although the radiative decay of the excited state is included, with the same value as before. Nuclear hyperfine depolarization is simulated for the $Q_1(2.5)$ transition. The hyperfine energy levels are calculated[42,43] for the relevant rotational, spin–orbit and Λ-doublet levels of the $X\,^2\Pi$ and $A\,^2\Sigma^+$ states using literature coupling constants.[44,45] The resulting simulation shows clear periodic oscillations. These oscillations show two separate frequencies. The higher of these arises from the $A\,^2\Sigma^+$ state and has a period of ≈2.4 ns, the lower from the $X\,^2\Pi$ state having a period of ≈8.6 ns. These different time scales simply reflect the different hyperfine coupling constants in these states. Each of these oscillations is a sine function, resulting from the two nuclear hyperfine levels in each of the ground and excited states.

The second simulation shown in Fig. 7, given by the dashed line, is identical to the first except for the laser pulse-

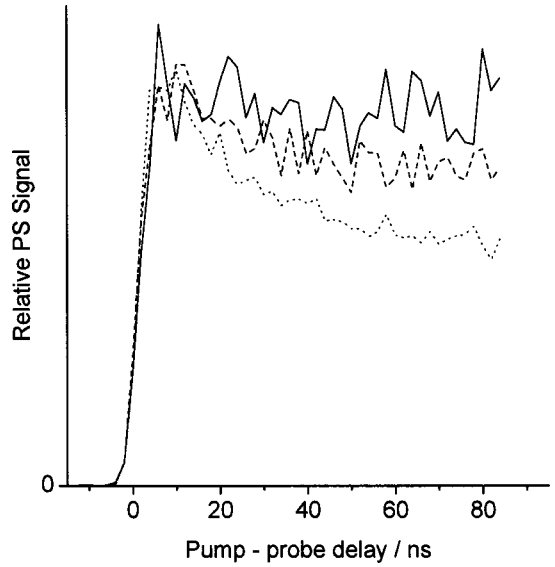

FIG. 8. Simulation of PS of OH $A\,^2\Sigma^+ - X\,^2\Pi$ (0,0) $Q_1(2.5)$ as a function of pump–probe delay showing influence of velocity changing collisions for different pump laser bandwidths. He collider number density of 3.24×10^{16} cm^{-3}, velocity-changing collision cross section 100 Å^2. The simulations assumed no other decay processes and a translational temperature of 298 K. The probe laser bandwidth was 0.06 cm^{-1} in all simulations. Solid line, pump laser bandwidth 0.2 cm^{-1}; dashed line, pump laser bandwidth 0.1 cm^{-1}; dotted line, pump laser bandwidth 0.06 cm^{-1}.

width, which is increased to 5 ns. Instead of the previously clear oscillations at two different frequencies, this simulation shows only a slight modulation at the lower frequency. The laser pulsewidth is now too broad to observe the high frequency oscillation from the $A\,^2\Sigma^+$ state. The width of the laser pulse has also largely averaged out the lower frequency oscillations from the $X\,^2\Pi$ state. These simulations show that with typical ns-pulsed dye lasers, hyperfine nuclear depolarization will not generally be observable for OH $A\,^2\Sigma^+ - X\,^2\Pi$ transitions in the form of oscillations as a function of pump–probe delay. They will however reduce the total signal level. Other species with different hyperfine coupling constants, and hence hyperfine depolarization timescales may produce measurable oscillations. For example, quantum beats from nuclear hyperfine interactions have been observed using time-resolved two-color resonant four-wave mixing in the ground $X\,^2\Pi$ and excited $A\,^2\Sigma^+$ states of NO.[39] In a one-color PS experiment on NO using ns-pulsed lasers we would expect to observe equivalent oscillations, with a combination of the frequencies observed for ground and excited states.

Finally, the effect of velocity-changing collisions is introduced in Fig. 8. These simulations assume no collisional or radiative relaxation, and ignore the influence of hyperfine depolarization. Velocity-changing collisions during the delay τ_2 are introduced in the following fashion. A collision cross section is assumed, for these simulations 100 Å^2, and the resulting collision rate calculated for He as a collider at a number density of 3.24×10^{16} cm^{-3} and temperature of 298 K. The probability densities of integer numbers of velocity-changing collisions are assumed to be distributed according to Poisson statistics. For each iteration of the MC procedure and assumed τ_2 the probability of at least one collision occurring is used in the usual MC fashion. If a collision does occurs, then a new velocity is MC selected from a 1D Maxwell–Boltzmann distribution, and is used in the subsequent calculation of the phase factor arising from delay τ_3. Laser bandwidths are introduced by MC selecting the pump and probe frequencies from separate Gaussian distributions centered at the transition frequency.

These additional dimensions in the MC integration required an increased number of iterations per simulation time step. We have chosen 1×10^9 as a reasonable compromise between statistical noise and computational time. Simulations for three pump laser bandwidths, 0.06 cm^{-1}, 0.1 cm^{-1}, and 0.2 cm^{-1}, are shown in Fig. 8. In each case, the probe laser bandwidth is assumed to be 0.06 cm^{-1}. A clear decrease in the PS signal as a function of pump–probe delay is seen for a pump bandwidth of 0.06 cm^{-1}, with a slower but discernible decrease for 0.1 cm^{-1}, and effectively no decrease on the experimental time scale for the 0.2 cm^{-1} pump bandwidth. This reflects the increasing proportion of the velocity distribution that is being excited as the pump laser bandwidth is increased. At 298 K the thermal OH velocity distribution gives a transition linewidth of $\approx$0.1 cm^{-1}. Thus, a pump bandwidth of 0.2 cm^{-1} pumps almost the entire velocity distribution.

IV. COMPARISON TO EXPERIMENT

In this section, we compare simulations produced using the procedure described in the preceding sections to representative experimentally measured PS signals. These preliminary measurements were made on the OH radical using the $A\,^2\Sigma^+ - X\,^2\Pi(0,0)$ transition. A more comprehensive series of measurements of OH collisional polarization properties will be reported in a later publication.

A. Experimental procedure

The experimental apparatus is practically the same as that described in a previous publication,[16] with the significant addition of another Nd:YAG pumped pulsed dye laser system. Only the essential details and differences are reported here.

OH $X\,^2\Pi$ radicals were generated by the 266 nm photodissociation of H_2O_2. The H_2O_2 (50% by weight with H_2O) was picked up by a flow of the collider gas, He. A total pressure of $\approx$600 mTorr was maintained in the cell by varying the flow rate, as monitored by a capacitance manometer (MKS). Three independent laser systems were used in the experiment, the relative timings of which were controlled by two digital delay generators [Stanford Research Systems (SRS) DG535]. The first laser, an Nd:YAG (Continuum Surelite II-10), generated 266 nm which was used to photodissociate the H_2O_2. The second laser system was a Nd:YAG pumped dye laser, (Lumonics Hyperdye/R640 laser dye), which produced doubled output at $\approx$308 nm suitable for the OH $A\,^2\Pi - X\,^2\Sigma^+$ (0,0) transition. This acted as the pump laser system. The final system was another Nd:YAG laser (Continuum Surelite II-10/Sirah Cobrastretch/R640 laser dye) which also generated doubled output at $\approx$308 nm. This system acted as the probe laser. The pump laser fired 8

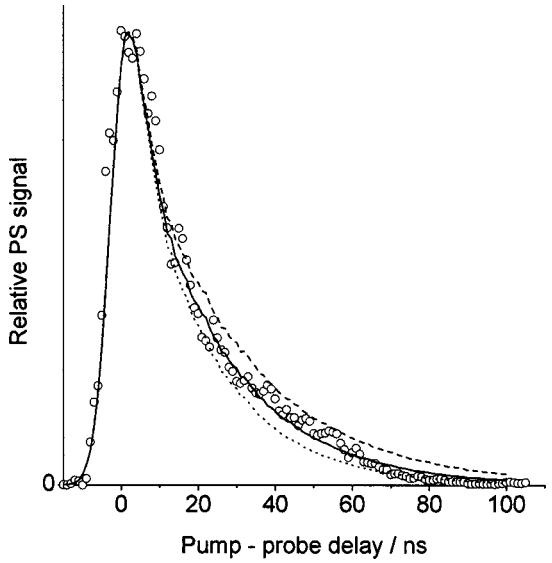

FIG. 9. Experimental data and simulation of PS of OH $A\,^2\Sigma^+ - X\,^2\Pi$ (0,0) $Q_1(2.5)$ as a function of pump–probe delay. Linear pump laser polarization, total pressure of H_2O_2/H_2O precursor, and He collider, 600 mTorr. Simulations assumed a 13 ns pump laser pulsewidth and a 5 ns probe laser pulsewidth, a radiative decay rate $k_{rad}=1.45\times10^6\ s^{-1}$, no velocity-changing collisions and a translational temperature of 298 K. Open circles, experimental data; dashed line, simulation assuming $k=0.9\times10^{-9}\ cm^3\,s^{-1}$; solid line, simulation assuming $k=1.1\times10^{-9}\ cm^3\,s^{-1}$; dotted line, simulation assuming $k=1.3\times10^{-9}\ cm^3\,s^{-1}$.

μs after the photolysis laser, sufficient time for the nascent OH translational distribution to relax to thermal equilibrium and for the nascent rotational distribution to be largely thermalized. The probe laser also fired at ≈8 μs after the photolysis laser, with the exact timing determining the pump–probe delay. This was scanned using the digital delay generator, typically from -20 ns to $+100$ ns.

PS was performed in a copropagating geometry with linear polarized pump light. The pump laser fluence was attenuated to ensure operation in the perturbative regime, as shown in a previous publication.[16] Stress induced birefringence in the cell windows alters the polarization of the probe beam and generates a wavelength-independent background signal. This was minimized before each experiment by careful application of a compensating stress to the cell through its mounting clamps. The pump and probe laser fluences were monitored using energy meters (Molectron). LIF was monitored through the cell side window and used to ensure that each of the pump and probe lasers was resonant with the desired transition. Both PS and LIF signals, and the output of the two energy monitors were passed to boxcar integrators (SRS SR250) and via a computer interface (SRS SR245) to a PC. The laser timing and probe laser wavelength, together with the data acquisition, were all controlled via LABVIEW software.

B. Comparison of simulations to experimental results

Figure 9 shows the variation with pump–probe delay of the experimentally measured PS signals from the OH $Q_1(2.5)$ transition with linearly polarized pump light. It is compared to three simulations. The simulations assumed thermal 298 K OH velocities, a 13 ns pulsewidth for the pump laser system, and a 5 ns pulsewidth for the probe laser, consistent with manufacturers' data. The assumed radiative decay rate of the excited state was $k_{rad}=1.45\times10^6\ s^{-1}$. Velocity-changing collisions were not included, for the reasons discussed in Sec. III B above. The simulations assume that the collisional rate constants for the ground and excited states are equal, at $0.9\times10^{-9}\ cm^3\,s^{-1}$, $1.1\times10^{-9}\ cm^3\,s^{-1}$, and $1.3\times10^{-9}\ cm^3\,s^{-1}$, respectively. The simulations clearly fit the data well, reproducing both the growth and decline of the experimental signal. As discussed in Sec. III B, the growth of the signal is defined by the pulsewidths of the pump and probe lasers. The decay of the signal is determined by the collisional loss of the population and the alignment created by the pump laser, as discussed in Sec. II C. The simulation assuming $1.1\times10^{-9}\ cm^3\,s^{-1}$ fits the experimental data best, with the other simulations giving an indication of the statistical, but not necessarily systematic, uncertainty in this measurement of about $1\times10^{-10}\ cm^3\,s^{-1}$.

Rate constants for the total loss processes occurring in the ground and excited states can be calculated from literature measurements of the rotational energy transfer (RET) and electronic quenching rate constants. The total pressure of collider and precursor gases in the experiment was 600 mTorr, of which we deduce that approximately 100 mTorr is the precursor H_2O_2/H_2O mixture (majority H_2O) from an analysis of the LIF radiative lifetime. A total collisional loss rate of $6.7\times10^6\ s^{-1}$ is predicted for the gas mixture for the excited $^2\Sigma^+$ state including both total RET rates out of the probed level[46,47] and electronic quenching rates.[48] This may be converted to an apparent rate constant, in which we assume that all 600 mTorr of the collider was the same gas, of $k_{app}=3.4\times10^{-10}\ cm^3\,s^{-1}$. A similar prediction of the total collisional loss rate through RET in the ground $^2\Pi$ state[49,50] may be made, and is found to give a total rate of $6.2\times10^6\ s^{-1}$ and an apparent rate constant, $k_{app}=3.2\times10^{-10}\ cm^3\,s^{-1}$.

These apparent rate constants calculated for the total population loss processes in the ground and excited states are only approximately 1/3 of the magnitude of the bulk polarization decay rate constant required to correctly simulate the experimental data. Two possible processes that may account for this are velocity-changing collisions, and angular momentum realignment. We do not believe that velocity-changing collisions are likely to be a major loss process in these experiments. The bandwidths of the pump and probe lasers are a significant fraction of the total Doppler width, being $\approx0.1\ cm^{-1}$ and $\approx0.06\ cm^{-1}$ FWHM, respectively. The simulations presented in Sec. III suggest that under these circumstances, even when assuming complete thermalization of velocities on every collision and a large cross section, no significant signal decay will occur on the experimental time scale. We are therefore led to the important conclusion that the observed rapid signal decay is the result of realignment of the rotational angular momentum and the consequent depolarization of the sample, with a second order rate constant, $k_{align}\approx7\times10^{-10}\ cm^3\,s^{-1}$.

There have been a number of previous measurements of depolarization of rotational angular momentum, using

optical-optical double resonance techniques. Studies prior to 1986 are summarized in the review article by McCaffery *et al.*[51] In some cases, depolarization has been found to be considerably slower than RET, for example self-collisions of N_2 $(v=1)$,[52] of CO,[53] and C_2H_2.[54] Other systems have produced significantly faster depolarization rates, notably $H_2(B\,^1\Sigma_u^+)$ with He, where depolarization of $J=1$, $m_J=0$ was found to have a cross section of 30 Å^2.[55] These variations may have several explanations. Depolarization is generally found to be significantly faster for lower *J*. This is not surprising, as a given absolute change in the magnitude of $|m_J|$ will result in a much larger proportional change in degree of orientation or alignment at low *J*. Second, and of more significance in dynamics, the shape of the potential will have a strong influence. For example, the $H_2(B\,^1\Sigma_u^+)-$He potential is strongly anisotropic, being repulsive in a linear geometry, but attractive in the ''T-shape'' geometry. The large reorientation cross section observed is attributed to this anisotropy, in contrast to $H_2(X\,^1\Sigma_g^+)-$He, where the potential is effectively isotropic and little reorientation is seen.

The most directly relevant studies to compare with our current data are FWM and PS measurements of OH, in atmospheric pressure flames. Williams *et al.*[25] measured FWM line shapes of OH $A\,^2\Sigma^+-X\,^2\Pi$ in $H_2/O_2/$He flames using different polarizations and derived line-broadening parameters for population and alignment relaxation rates. A notable finding for the two low *J* transitions studied, $Q_{21}(1.5)$ and $Q_{21}(3.5)$, was that the polarization relaxation rate was almost twice the measured population relaxation rate. The flame conditions are clearly very different (atmospheric pressure and 1380 K) from our room temperature, low pressure experiments. However, neglecting any dependence of the collision cross sections on temperature we can convert these line broadening parameters to rate constants for the flame conditions, and then to equivalent rate constants at room temperature. The resulting predicted rate constants are, for population decay, $k_{\mathrm{pop}}=3.3\times10^{-10}$ cm^3 s^{-1}, and for alignment decay, $k_{\mathrm{align}}=6.4\times10^{-10}$ cm^3 s^{-1}.

The decay of FWM and PS signals has also been studied independently by Drier and co-workers using picosecond lasers on the OH $A\,^2\Sigma^+-X\,^2\Pi$ transition in $CH_4/$air and H_2/O_2 atmospheric pressure flames. Population, orientation and alignment decay were measured for a range of *J*.[12–15] The general trends found were that orientation relaxes slower than alignment, and for both, relaxation slows with increasing *J*. FWM measurements on the $Q_1(1.5)$ transition yielded both population and orientation decay rates, and the orientation was seen to decay faster than the population, in agreement with the observations of Williams *et al.* A conversion of these decay rates to equivalent second order collision rates at room temperature assuming equivalent collision cross sections and a H_2/O_2 flame at a temperature of 1600 K, yields a population decay rate, $k_{\mathrm{pop}}=4.4\times10^{-10}$ cm^3 s^{-1}, and an orientation decay rate, $k_{\mathrm{or}}=6.5\times10^{-10}$ cm^3 s^{-1}.

The correspondence between our new measured values and these estimates from both Williams *et al.* and Suvernev *et al.* is striking. Under Williams *et al.*'s conditions the flame composition is estimated to be 3% O_2, 24% H_2O, and 73% He, not markedly different from our gas composition, deduced to be 17% H_2O and 83% He. Our measurements therefore appear to confirm the findings of Williams *et al.* that elastic reorientating collisions are favored over RET collisions at low *J* for OH with He as a collider.

In a future paper, we will present further measurements of OH collisions using one-color PS, exploring the influence of different collision partners and varying rotational quantum number. One limitation of one-color PS is that both the ground and excited states contribute to the signal together, as does the decay of the prepared polarization in both levels. This may be overcome using two-color PS, probing on a different transition to that used in the pump stage. Two-color PS may be analyzed in a precisely analogous fashion to the one-color PS derivation presented in this paper, and will be the subject of a future publication.[56]

V. CONCLUSIONS

The motivation behind this work has been the desire to measure rotational angular momentum relaxation and transfer in inelastic collisions of electronically excited small free radicals. This paper has described an angular momentum tensor moment analysis of the signals arising in one-color PS, in which the process of keeping track of the time-ordered sequence of interactions is simplified by the use of double-sided Feynman diagrams. Unlike previous related work on FWM, we do not assume that collisional decay rates are rapid with respect to the laser pulsewidth, nor do we assume that decay rates are independent of the m_J level. The result shows that when the pump and probe lasers are well separated in time, the pump laser prepares either orientation or alignment of the rotational angular momentum in the resonant rotational levels, depending on the pump polarization. The signal is generated by the interaction of the probe laser with this oriented or aligned sample, and is sensitive to the decay of both the populations of the probed levels and the anisotropy of the rotational angular momentum. If the collisional population transfer rates are known from other measurements, then the rate of loss of angular momentum orientation or alignment can be inferred directly.

We have also analyzed the influence of other processes, including the Doppler motion of the probed molecules, the effect of velocity-changing collisions, and of nuclear hyperfine depolarization. The Doppler motion of the sample introduces a dephasing process during delays following an odd number of photon interactions. As a result, the growth of the PS signal closely follows the overlap of the pump and probe lasers. For the same reason, the signal pulse follows closely the temporal profile of the probe laser. Nuclear hyperfine depolarization during the pump–probe delay was introduced to the analysis using the standard literature description of angular momentum depolarization. The resulting oscillations of the prepared orientation and alignment prove to be too rapid to be measured using commercial ns-pulsed lasers in the current example of the OH $A\,^2\Sigma^+-X\,^2\Pi$ transition. Velocity-changing collisions are predicted to reduce the absolute magnitude of the measured signals when they occur during the τ_1 and τ_3 periods, by introducing an additional dephasing process. The effect of velocity-changing collisions

during the second delay period is distinct and less pronounced. Assuming the laser bandwidth is less than the Doppler width, a velocity subgroup is pumped, and subsequently probed, subject to resonance conditions with the pump and probe lasers. Only collisions that change the velocity sufficiently to destroy this resonance condition result in signal decay. With common commercial ns-pulsed dye laser systems the typical laser bandwidth will cover most of the thermal Doppler width, and such collisional effects will be relatively unimportant.

Preliminary measurements of a representative PS signal from OH in collision with He were made on the $Q_1(2.5)$ transition of the $A\,^2\Sigma^+ - X\,^2\Pi$ (0,0) band. These measurements were compared to simulations, and the rate constants required to reproduce the experimental data deduced. The results were discussed in terms of literature RET and quenching rates. The striking finding is that a realignment rate of approximately twice the RET and quenching rates is required to accurately model the data. This is in satisfactory agreement with previous ps-pulsed PS and FWM measurements in flames[13–15] and with FWM line shape measurements in He-rich flames.[25] These measurements thus support the conclusion that polarization decay is faster than RET for low J OH.

ACKNOWLEDGMENTS

We thank the EPSRC for a research grant including a studentship for H.J.C. M.L.C. thanks the Royal Society of Edinburgh for a BP Research Fellowship.

APPENDIX: PERTURBATIVE DERIVATION OF PS SIGNAL

In this Appendix the derivation of the functional form for the electric field arising from Feynman diagram IA of Fig. 1 is outlined in detail. The rules for determining the operators for a particular interaction in the Feynman diagram are given in Ref. 29. Equations (A1)–(A3) list the perturbation Hamiltonians for the three separate photon interactions shown in Fig. 1, diagram IA,

$$\frac{H^{(1)}(t_1)}{i\hbar} = -\frac{1}{2i\hbar}(\boldsymbol{\mu}\cdot\boldsymbol{\varepsilon}_1)\xi_1 e^{-i\omega_1 t_1 + i\mathbf{k}_1\cdot\mathbf{r}}, \tag{A1}$$

$$\frac{H^{(2)}(t_2)}{i\hbar} = -\frac{1}{2i\hbar}(\boldsymbol{\mu}\cdot\boldsymbol{\varepsilon}_2^*)\xi_2 e^{+i\omega_2 t_2 - i\mathbf{k}_2\cdot\mathbf{r}}, \tag{A2}$$

$$\frac{H^{(3)}(t_3)}{i\hbar} = -\frac{1}{2i\hbar}(\boldsymbol{\mu}\cdot\boldsymbol{\varepsilon}_3)\xi_3 e^{-i\omega_3 t_3 + i\mathbf{k}_3\cdot\mathbf{r}}. \tag{A3}$$

The initial sample is assumed to be thermalized, with a uniform m_J state population distribution in the ground state, and no population in the excited state. The resulting initial density matrix, at time t_1, is nonzero only along the diagonal,

$$\rho^{(0)}(t_1) = \sum_{m_g} \frac{|J_g m_g\rangle\langle J_g m_g|}{(2J_g+1)}. \tag{A4}$$

The first perturbation Hamiltonian, (A1), is now applied to give the first order density matrix. The diagram shows that this acts from the left, on the ket space, and accordingly the first order density matrix can be written as

$$\rho^{(1)}(t_1) = \frac{-\xi_1 e^{-i\omega_1 t_1 + i\mathbf{k}_1\cdot\mathbf{r}}}{2i\hbar(2J_g+1)} \times \sum_{m_g, m_e} |J_e m_e\rangle\langle J_e m_e|\boldsymbol{\mu}\cdot\boldsymbol{\varepsilon}_1|J_g m_g\rangle\langle J_g m_g|. \tag{A5}$$

The tensor dot product ($\boldsymbol{\mu}\cdot\boldsymbol{\varepsilon}$) can be expressed in the spherical basis, and the Wigner–Eckart theorem applied to the resulting matrix element.[32] This gives the following expanded form:

$$\rho^{(1)}(t_1) = \frac{-\xi_1 e^{-i\omega_1 t_1 + i\mathbf{k}_1\cdot\mathbf{r}}\langle J_e\|(\mu_1)^{(1)}\|J_g\rangle}{2i\hbar(2J_g+1)} \times \sum_{m_g, m_e, P_1} (-1)^{P_1 + J_e - m_e}(\varepsilon_1)^{(1)}_{-P_1} \times \begin{pmatrix} J_e & 1 & J_g \\ -m_e & P_1 & m_g \end{pmatrix} |J_e m_e\rangle\langle J_g m_g|. \tag{A6}$$

The density matrix operators can be expressed in a spherical basis in terms of the spherical tensor operators $T^{K_1}_Q(J_e J_g)$ as defined by Blum[33]

$$|J_e m_e\rangle\langle J_g m_g| = \sum_{K_1, Q_1} (-1)^{J_e - m_e}(2K_1+1)^{1/2} \times \begin{pmatrix} J_e & J_g & K_1 \\ m_e & -m_g & -Q_1 \end{pmatrix} T^{K_1}_{Q_1}(J_e J_g). \tag{A7}$$

Substituting Eq. (A7) into Eq. (A6) and using the orthogonality of the 3-j symbols we find

$$\rho^{(1)}(t_1) = \frac{-\xi_1 e^{-i\omega_1 t_1 + i\mathbf{k}_1\cdot\mathbf{r}}\langle J_e\|(\mu_1)^{(1)}\|J_g\rangle}{2i\hbar(2J_g+1)} \times \sum_{K_1, Q_1, P_1} \frac{(-1)^{P_1}(\varepsilon_1)^{(1)}_{-P_1} T^{K_1}_{Q_1}(J_e J_g)\delta_{K_1,1}\delta_{Q_1,P_1}}{(2K_1+1)^{1/2}}. \tag{A8}$$

The Kroenecker delta functions in Eq. (A8) indicate that the expression is nonzero only when $K_1 = 1$ and $Q_1 = P_1$.

We now consider the time evolution of the density matrix in the interval τ_1 between t_1 and t_2. The matrix can be described at any time by an expansion in the spherical tensor operators and state multipoles. The time evolution of the density matrix is contained within the state multipoles. If the collisional environment is isotropic then all projections, Q, of a given multipole moment rank, K, evolve with the same rate.[33] Including the energy propagator, which is independent of the multipole rank, the density matrix at time t_2 before the interaction with the second photon can be written as

$$\rho^{(1)}(t_2)=e^{-i\omega_{J_eJ_g}\tau_1}\sum_{K_1,Q_1}\rho^{K_1}_{Q_1}(J_eJ_g)T^{K_1}_{Q_1}(J_eJ_g)e^{-\Gamma_{K_1}\tau_1}. \quad \text{(A9)}$$

It was noted above that the only nonzero result is for $K_1=1$, assured by the delta function in Eq. (A8). Hence only one state multipole is nonzero. There is only a single decay rate to consider, involving the off-diagonal elements of a density matrix between ground and excited states. We henceforth denote this dephasing rate constant as Γ_d, and the resulting first order density matrix at time t_2 is

$$\rho^{(1)}(t_2)=\frac{-\xi_1 e^{-i\omega_1 t_1+i\mathbf{k}_1\cdot\mathbf{r}}e^{-i\omega_{J_eJ_g}\tau_1}e^{-\Gamma_d\tau_1}\langle J_e\|(\mu_1)^{(1)}\|J_g\rangle}{2i\hbar(2J_g+1)}\times\sum_{Q_1}\frac{(-1)^{Q_1}(\varepsilon_1)^{(1)}_{-Q_1}T^1_{Q_1}(J_eJ_g)}{\sqrt{3}}. \quad \text{(A10)}$$

We can now proceed with the second optical interaction. We expand the spherical tensor operator, as defined by Blum,[33] once again

$$T^k_q(J'J)=\sum_{m',m}(-1)^{J'-m'}(2k+1)^{1/2}\begin{pmatrix}J' & J & k\\ m' & -m & -q\end{pmatrix}|J'm'\rangle\langle J,m|, \quad \text{(A11)}$$

then apply the second photon interaction Hamiltonian to yield

$$\rho^{(2)}(t_2)=\frac{-\xi_1\xi_2 e^{-i(\omega_1t_1+\omega_2t_2)}e^{i(\mathbf{k}_1-\mathbf{k}_2)\cdot\mathbf{r}}e^{-i\omega_{J_eJ_g}\tau_1}e^{-\Gamma_d\tau_1}\langle J_e\|(\mu_1)^{(1)}\|J_g\rangle}{4\hbar^2(2J_g+1)}\times\sum_{Q_1}(-1)^{Q_1}(\varepsilon_1)^{(1)}_{-Q_1}\sum_{m_e,m_g,m_{g'}}(-1)^{J_e-m_e}\begin{pmatrix}J_e & J_g & 1\\ m_e & -m_g & -Q_1\end{pmatrix}|J_gm_{g'}\rangle\langle J_gm_{g'}|(\boldsymbol{\mu}\cdot\boldsymbol{\varepsilon}^*)|J_em_e\rangle\langle J_gm_g|. \quad \text{(A12)}$$

The further steps applied to the first order density matrix can now be applied again. After some rearrangement of the 3-j symbols to simplify the result we find

$$\rho^{(2)}(t_2)=\frac{-\xi_1\xi_2 e^{-i(\omega_1t_1+\omega_2t_2)}e^{i(\mathbf{k}_1-\mathbf{k}_2)\cdot\mathbf{r}}e^{-i\omega_{J_eJ_g}\tau_1}e^{-\Gamma_d\tau_1}\langle J_e\|(\mu_1)^{(1)}\|J_g\rangle\langle J_g\|(\mu_2)^{(1)}\|J_e\rangle}{4\hbar^2(2J_g+1)}\times\sum_{K_2,Q_1,Q_2}(-1)^{K_2+2J_g}(\varepsilon_1)^{(1)}_{-Q_1}(\varepsilon_2^*)^{(1)}_{Q_1-Q_2}(2K_2+1)^{1/2}\begin{Bmatrix}1 & J_g & J_e\\ J_g & 1 & K_2\end{Bmatrix}\begin{pmatrix}1 & 1 & K_2\\ Q_2-Q_1 & Q_1 & -Q_2\end{pmatrix}T^{K_2}_{Q_2}(J_gJ_g). \quad \text{(A13)}$$

Here we have succeeded in separating the geometrical and dynamical factors determining the signal. The 3-j symbol and light polarization tensors restrict K_2 to 0, 1 or 2, i.e., population, orientation or alignment, respectively. The 6-j symbol contains the sensitivity to spectroscopic branch. Equation (A13) could equally well be written in terms of angular momentum alignment operators, as discussed in Sec. II C.

The second order density matrix evolves during the delay $\tau_2=t_3-t_2$. Crucially, because the states involved are degenerate the only term in the evolution arises from collisional processes,

$$\rho^{(2)}(t_3)=\rho^{(2)}(t_2)e^{-\Gamma^{J_g}_{K_2}(t_3-t_2)}. \quad \text{(A14)}$$

We include this decay rate, dependent on the spherical tensor rank K_2, and apply the third photon interaction at time t_3. Exactly the same procedure as with the previous two interaction Hamiltonians followed by a similar angular momentum rearrangement leads to

$$\rho^{(3)}(t_3)=\frac{\xi_1\xi_2\xi_3 e^{-i(\omega_1t_1+\omega_2t_2-\omega_3t_3)}e^{i(\mathbf{k}_1-\mathbf{k}_2+\mathbf{k}_3)\cdot\mathbf{r}}e^{-i\omega_{J_eJ_g}\tau_1}e^{-\Gamma_d\tau_1}\langle J_e\|(\mu_1)^{(1)}\|J_g\rangle\langle J_g\|(\mu_2)^{(1)}\|J_e\rangle\langle J_e\|(\mu_3)^{(1)}\|J_g\rangle}{8i\hbar^3(2J_g+1)}$$

$$\times\sum_{K_2,K_3,Q_1,Q_2,Q_3}(-1)^{1+K_2+3J_g+J_e}(\varepsilon_1)^{(1)}_{-Q_1}(\varepsilon_2^*)^{(1)}_{Q_1-Q_2}(\varepsilon_3)^{(1)}_{Q_2-Q_3}$$

$$\times\begin{Bmatrix}1 & J_g & J_e\\ J_g & 1 & K_2\end{Bmatrix}\begin{pmatrix}1 & 1 & K_2\\ Q_2-Q_1 & Q_1 & -Q_2\end{pmatrix}e^{-\Gamma^{J_g}_{K_2}(t_3-t_2)}(2K_2+1)(2K_3+1)^{1/2}$$

$$\times\begin{Bmatrix}K_2 & J_g & J_g\\ J_e & K_3 & 1\end{Bmatrix}\begin{pmatrix}K_3 & K_2 & 1\\ Q_3 & -Q_2 & Q_2-Q_3\end{pmatrix}T^{K_3}_{Q_3}(J_eJ_g). \quad \text{(A15)}$$

The final time evolution of the system is during delay $\tau_3 = t - t_3$. This introduces a final decay rate giving the density matrix

$$\rho^{(3)}(t) = \rho^{(3)}(t_3) e^{-\Gamma_{K_3}\tau_3} e^{-i\omega_{J_e J_g}\tau_3}. \tag{A16}$$

The observed signal depends on the electric field generated by the third-order nonlinear polarization represented by this density matrix. This electric field can be found as the expectation of the dipole operator acting on the density matrix,[23]

$$\mathbf{P}^{(3)}(t)\cdot\boldsymbol{\varepsilon}_4^* = N\,\mathrm{Tr}\{\rho^{(3)}(t)\cdot(\boldsymbol{\mu}\cdot\boldsymbol{\varepsilon}_4^*)\},$$

$$\mathbf{P}^{(3)}(t)\cdot\boldsymbol{\varepsilon}_4^* = N\sum_{m_g}\langle J_g m_g|\rho^{(3)}(t)\cdot(\boldsymbol{\mu}\cdot\boldsymbol{\varepsilon}_4^*)|J_g m_g\rangle, \tag{A17}$$

where N is the total number of molecules present. Writing the density matrix as an expansion in state multipoles gives

$$\mathbf{P}^{(3)}(t)\cdot\boldsymbol{\varepsilon}_4^* = N\sum_{K_3,Q_3,m_{e'},m_g}\rho_{Q_3}^{K_3}(t)(-1)^{J_e-m_{e'}}(2K_3+1)^{1/2} \times\begin{pmatrix} J_e & J_g & K_3 \\ m_{e'} & -m_g & -Q_3 \end{pmatrix} \times\langle J_g m_g|\boldsymbol{\mu}\cdot\boldsymbol{\varepsilon}_4^*|J_e m_{e'}\rangle\langle J_g m_g|J_g m_g\rangle. \tag{A18}$$

The dipole operator can once again be expressed in the spherical basis and the Wigner–Eckart theorem applied. The orthogonality of the 3-j symbols restricts the nonzero value of K_3 to unity and the signal photon polarization spherical tensor projection to Q_3. The relaxation during delay τ_3 is physically the same process as during delay τ_1 and thus $\Gamma_{K_3}=\Gamma_d$. Hence, the electric field associated with the time-ordered sequence of photon interactions described by Feynman diagram IA is finally

$$\begin{aligned}\mathbf{P}^{(3)}(t)\cdot\boldsymbol{\varepsilon}_4^* = {}& \frac{N\xi_1\xi_2\xi_3 e^{-i(\omega_1 t_1-\omega_2 t_2+\omega_3 t_3)} e^{i(\mathbf{k}_1-\mathbf{k}_2+\mathbf{k}_3)\cdot\mathbf{r}} e^{-i\omega_{J_e J_g}(\tau_1+\tau_3)} e^{-\Gamma_d(\tau_1+\tau_3)}}{8i\hbar^3(2J_g+1)} \\ &\times|\langle J_e\|(\mu)^{(1)}\|J_g\rangle|^4\sum_{K_2}\begin{Bmatrix} 1 & J_g & J_e \\ J_g & 1 & K_2 \end{Bmatrix}^2 e^{-\Gamma_{K_2}^{J_g}\tau_2} \\ &\times\sum_{Q_1,Q_2,Q_3}(-1)^{Q_2}(2K_2+1)(\varepsilon_1)_{-Q_1}^{(1)}(\varepsilon_2^*)_{Q_1-Q_2}^{(1)}(\varepsilon_3)_{Q_2-Q_3}^{(1)}(\varepsilon_4^*)_{Q_3}^{(1)} \\ &\times\begin{pmatrix} 1 & 1 & K_2 \\ Q_2-Q_1 & Q_1 & -Q_2 \end{pmatrix}\begin{pmatrix} 1 & 1 & K_2 \\ Q_2-Q_3 & Q_3 & -Q_2 \end{pmatrix}. \end{aligned} \tag{A19}$$

The phase factor in Eq. (A19) may be rewritten in terms of delays, τ_n, resulting in the functional forms given in Eqs. (1)–(7).

[1] C. Wieman and T. W. Hänsch, Phys. Rev. Lett. **36**, 1170 (1976).
[2] K. Nyholm, Opt. Commun. **111**, 66 (1994).
[3] K. Nyholm, R. Fritzon, and M. Aldén, Opt. Lett. **18**, 1672 (1993).
[4] A. A. Suvernev, A. Dreizler, T. Dreier, and J. Wolfrum, Appl. Phys. B: Lasers Opt. **61**, 421 (1995).
[5] B. Löfstedt and M. Aldén, Opt. Commun. **124**, 251 (1996).
[6] K. Nyholm, M. Kaivola, and C. G. Aminoff, Appl. Phys. B: Lasers Opt. **60**, 5 (1995).
[7] T. A. Reichardt and R. P. Lucht, J. Chem. Phys. **109**, 5830 (1998).
[8] W. C. Giancola, T. A. Reichardt, and R. P. Lucht, J. Opt. Soc. Am. B **17**, 1781 (2000).
[9] S. Roy, T. A. Reichardt, and R. P. Lucht, J. Chem. Phys. **116**, 4030 (2002).
[10] T. A. Reichardt, W. C. Giancola, and R. P. Lucht, Appl. Opt. **39**, 2002 (2000).
[11] T. A. Reichardt, F. Di Teodoro, R. L. Farrow, S. Roy, and R. P. Lucht, J. Chem. Phys. **113**, 2263 (2000).
[12] A. Dreizler, R. Tadday, A. A. Suvernev, M. Himmelhaus, T. Dreier, and P. Foggi, Chem. Phys. Lett. **240**, 315 (1995).
[13] A. A. Suvernev, R. Tadday, and T. Dreier, Phys. Rev. A **58**, 4102 (1998).
[14] R. Tadday, A. A. Suvernev, T. Dreier, and J. Wolfrum, Chem. Phys. Lett. **268**, 117 (1997).
[15] R. Tadday, A. Dreizler, A. A. Suvernev, and T. Dreier, J. Math. Phys. **410–411**, 85 (1997).
[16] H. J. Crichton, M. L. Costen, and K. G. McKendrick, J. Chem. Phys. **119**, 9461 (2003).
[17] A. J. Orr-Ewing and R. N. Zare, in *Chemical Dynamics and Kinetics of Small Radicals*, Advances in Physical Chemistry Series edited by A. Wagner and K. Liu (World Scientific, Singapore, 1995).
[18] J. I. Cline, K. T. Lorenz, E. A. Wade, J. W. Barr, and D. W. Chandler, J. Chem. Phys. **115**, 6277 (2001).
[19] K. T. Lorenz, D. W. Chandler, J. W. Barr, W. Chen, G. L. Barnes, and J. I. Cline, Science **293**, 2063 (2001).
[20] C. J. Randall, C. Murray, and K. G. McKendrick, Phys. Chem. Chem. Phys. **2**, 461 (2000).
[21] C. Murray, C. J. Randall, and K. G. McKendrick, Phys. Chem. Chem. Phys. **2**, 5553 (2000).
[22] G. Richmond, M. L. Costen, and K. G. McKendrick (unpublished).
[23] S. Mukamel, *Principles of Nonlinear Optical Spectroscopy* (Oxford University Press, Oxford, 1995).
[24] S. Williams, L. A. Rahn, and R. N. Zare, J. Chem. Phys. **101**, 1072 (1994).
[25] S. Williams, L. A. Rahn, and R. N. Zare, J. Chem. Phys. **104**, 3947 (1996).
[26] T. A. W. Waserman, B. R. Johnson, and P. H. Vaccaro, J. Chem. Phys. **108**, 7713 (1998).
[27] T. A. Wasserman, P. H. Vaccaro, and B. R. Johnson, J. Chem. Phys. **106**, 6314 (1997).
[28] T. A. W. Wasserman, P. H. Vaccaro, and B. R. Johnson, J. Chem. Phys. **116**, 10099 (2002).
[29] T. K. Yee and T. K. Gustafson, Phys. Rev. A **18**, 1597 (1978).
[30] Peixian Ye and Y. R. Shen, Phys. Rev. A **25**, 2183 (1982).
[31] Y. Prior, IEEE J. Quantum Electron. **20**, 37 (1984).
[32] R. N. Zare, *Angular Momentum: Understanding Spatial Aspects in Chemistry and Physics* (Wiley, New York, 1988).
[33] K. Blum, *Density Matrix Theory and Applications* (Plenum, New York, 1996).
[34] P. R. Berman, T. W. Mossberg, and S. R. Hartmann, Phys. Rev. A **25**, 2550 (1982).
[35] R. Sung and P. R. Berman, Phys. Rev. A **39**, 6284 (1989).

[36] T. W. Mossberg, R. Kachru, and S. R. Hartmann, Phys. Rev. A **20**, 1976 (1979).
[37] P. R. Berman and W. E. Lamb, Jr., Phys. Rev. A **2**, 2435 (1970).
[38] Y. Tang, J. P. Schmidt, and S. A. Reid, J. Chem. Phys. **110**, 5734 (1999).
[39] E. F. McCormack and E. Sarajlic, Phys. Rev. A **63**, 023406 (2001).
[40] F. Di Teodoro and E. F. McCormack, J. Phys. B **32**, 4389 (1999).
[41] J. Luque and D. Crosley, LIFBASE: Database and Spectral Simulation Program (Version 1.61) (SRI International, 1999).
[42] G. C. Dousmanis, T. M. Sanders, Jr., and C. H. Townes, Phys. Rev. **100**, 1735 (1955).
[43] C. H. Townes and A. L. Schawlow, *Microwave Spectroscopy* (Dover, New York, 1955).
[44] J. J. Ter Meulen, W. A. Majewski, W. L. Meerts, and A. Dynamus, Chem. Phys. Lett. **94**, 25 (1983).
[45] P. Kristiansen and L. Veseth, J. Chem. Phys. **84**, 2711 (1986).
[46] A. Jorg, U. Meier, R. Kienle, and K. Kohse-Höinghaus, Appl. Phys. B: Photophys. Laser Chem. **55**, 305 (1992).
[47] A. Jorg, U. Meier, and K. Kohse-Höinghaus, J. Chem. Phys. **93**, 6453 (1990).
[48] A. E. Bailey, D. E. Heard, D. A. Henderson, and P. H. Paul, Chem. Phys. Lett. **302**, 132 (1999).
[49] K. M. Hickson, C. M. Sadowski, and I. W. M. Smith, J. Phys. Chem. A **106**, 8442 (2002).
[50] K. M. Hickson, C. M. Sadowski, and I. W. M. Smith, Phys. Chem. Chem. Phys. **4**, 5613 (2002).
[51] A. J. McCaffery, M. J. Proctor, and B. J. Whitaker, Annu. Rev. Phys. Chem. **37**, 223 (1986).
[52] G. O. Sitz and R. L. Farrow, J. Chem. Phys. **101**, 4682 (1994).
[53] Ph Bréchignac, A. Picard-Bersellini, and R. Charneau, J. Phys. B **13**, 135 (1980).
[54] A. D. Rudert, J. Martin, Wen-Biu Gao, H. Zacharias, and J. B. Halpern, J. Chem. Phys. **112**, 9749 (2000).
[55] C. D. Pibel and C. B. Moore, J. Chem. Phys. **93**, 4804 (1990).
[56] M. L. Costen, H. J. Crichton, and K. G. McKendrick (unpublished).